

PNNL-33476, Rev 0
DVZ-RPT-086, Rev 0

Alternative Conceptual Models of the Subsurface at the Hanford Site

September 2022

Mark L Rockhold
Xiaoliang He

DISCLAIMER

This report was prepared as an account of work sponsored by an agency of the United States Government. Neither the United States Government nor any agency thereof, nor Battelle Memorial Institute, nor any of their employees, makes **any warranty, express or implied, or assumes any legal liability or responsibility for the accuracy, completeness, or usefulness of any information, apparatus, product, or process disclosed, or represents that its use would not infringe privately owned rights.** Reference herein to any specific commercial product, process, or service by trade name, trademark, manufacturer, or otherwise does not necessarily constitute or imply its endorsement, recommendation, or favoring by the United States Government or any agency thereof, or Battelle Memorial Institute. The views and opinions of authors expressed herein do not necessarily state or reflect those of the United States Government or any agency thereof.

PACIFIC NORTHWEST NATIONAL LABORATORY
operated by
BATTELLE
for the
UNITED STATES DEPARTMENT OF ENERGY
under Contract DE-AC05-76RL01830

Printed in the United States of America

Available to DOE and DOE contractors from
the Office of Scientific and Technical Information,
P.O. Box 62, Oak Ridge, TN 37831-0062

www.osti.gov

ph: (865) 576-8401

fox: (865) 576-5728

email: reports@osti.gov

Available to the public from the National Technical Information Service
5301 Shawnee Rd., Alexandria, VA 22312

ph: (800) 553-NTIS (6847)

or (703) 605-6000

email: info@ntis.gov

Online ordering: <http://www.ntis.gov>

Alternative Conceptual Models of the Subsurface at the Hanford Site

September 2022

Mark L Rockhold
Xiaoliang He

Prepared for
the U.S. Department of Energy
under Contract DE-AC05-76RL01830

Pacific Northwest National Laboratory
Richland, Washington 99354

Executive Summary

This report describes the use of a multipoint geostatistics (MPS) framework with multiple data types for developing alternative conceptual-mathematical models of the subsurface at the Hanford Site. Developing multiple conceptual-mathematical models of the site is important for assessing potential uncertainties related to the features, events, and processes that control the subsurface flow of groundwater and the transport of contaminants of concern (COCs). Evaluating the effects of these uncertainties can result in better site characterization, monitoring, and remedial decisions.

Contaminant plume maps suggest that paleochannels have a strong influence on subsurface flow and transport behavior at the Hanford Site. Recent surface-based geophysical data provide additional evidence for paleochannel features in some areas. The primary focus of this work is on developing an approach for evaluating the potential effects of paleochannel features on subsurface flow and contaminant transport. The multiple data types that were used in this study include grain-size distribution, electrical resistivity tomography (ERT), and Light Detection and Ranging (LiDAR)-based digital elevation data. The LiDAR data show outlines of relic paleochannel features that were formed by the ancestral Columbia River and flooding events in the past. These relic paleochannel features were assumed to be representative of paleochannel features that exist in the subsurface. The use of this combination of data in an MPS framework for generating realizations of paleochannel features at the Hanford Site is unique.

A training image used by the MPS algorithm was developed from the LiDAR-based digital elevation data. Binned grain-size distribution metrics from selected borehole samples, and ERT data from selected measurement transects, were also used, as hard (known) and soft (uncertain) categorical data, respectively, for representing paleochannel features in the MPS algorithm. The methodology reproduces the general shapes of the relic paleochannel features visible in the LiDAR-based topography data and honors the hard data at their measurement locations.

Multiple realizations of paleochannel features were generated and superimposed on a base or reference model. The alternative models were implemented numerically using the subsurface flow and transport simulator eSTOMP (<https://www.pnnl.gov/estomp>). Simulations were performed of the transport of three COCs – tritium, carbon tetrachloride, and iodine-129 – using the alternative conceptual models, and a base or reference case that was developed from the Plateau-to-River (P2R) model of the Hanford Site.¹

The alternative models containing paleochannel features generated by the MPS algorithm produced slightly faster transport results relative to the base model, but the general trajectories of the centers of mass of the simulated plumes were very similar for all of the models. It is anticipated that larger variations in transport results would occur with more alternative model realizations, and if different methods were used for parameterization of the material properties assigned to the paleochannel features.

The described methodology provides a systematic approach for using multiple types of site characterization data to develop alternative conceptual-mathematical models of the subsurface that include paleochannels. The models developed using this approach are consistent with all available characterization data used in their development. Using the alternative models for subsurface flow and transport modeling illustrates some of the potential effects of uncertainties in features such as paleochannels on the predicted transport and fate of selected COCs at Hanford. Assessment of these uncertainties can help to inform site characterization, monitoring, and remediation decisions.

¹ Budge, T. J. 2020. Model Package Report: Plateau to River Groundwater Model, Version 8.3. CP-57037, Rev. 2, CH2MHill Plateau Remediation Company, Richland, Washington.

Acknowledgments

Funding for this work was provided by the U.S. Department of Energy Richland Operations Office under the Deep Vadose Zone – Applied Field Research Initiative. The Pacific Northwest National Laboratory is operated by Battelle Memorial Institute for the Department of Energy under Contract DE-AC05-76RL01830. We thank Rob Mackley and Inci Demirkanli for project management and technical reviews, respectively, Steve Eklund for quality assurance review, and Matt Wilburn for editorial and text processing support.

Acronyms and Abbreviations

COC	contaminant of concern
CSM	conceptual site model
EC	electrical conductivity
ERT	electrical resistivity tomography
FY	fiscal year
GFM	geologic framework model
HCZ	high-conductivity zone
HEIS	Hanford Environmental Information System
LiDAR	Light Detection and Ranging (laser-based method used to determine ground surface elevations)
MCL	maximum concentration limit
MPS	multipoint geostatistics
NQAP	Nuclear Quality Assurance Program
P&T	pump-and-treat
P2R	Plateau-to-River
TI	training image

Contents

Executive Summary	ii
Acknowledgments.....	iii
Acronyms and Abbreviations	iv
Contents	v
1.0 Introduction.....	1.1
2.0 Background.....	2.1
3.0 Methods	3.1
3.1 Multipoint Geostatistics	3.1
3.1.1 Training Image	3.1
3.1.2 Hard Data.....	3.4
3.1.3 Soft Data.....	3.6
3.2 Flow and Transport Models.....	3.11
3.2.1 Grid.....	3.11
3.2.2 Material Type Distributions.....	3.12
3.2.3 Material Properties	3.16
3.2.4 Solutes	3.16
3.2.5 Initial and Boundary Conditions.....	3.20
4.0 Results and Discussion	4.1
4.1 Tritium	4.1
4.2 Carbon Tetrachloride	4.1
4.3 Iodine-129.....	4.9
4.4 Spatial Moment Analysis.....	4.14
5.0 Summary and Conclusions	5.1
6.0 Quality Assurance.....	6.1
7.0 References.....	7.1

Figures

Figure 3.1.	LiDAR-based ground surface elevation data (top), and outlines or areas defined by polylines representing relic paleochannel features (bottom). The shaded blue and green regions in the lower plot represent areas where relic paleochannel features are observable in the LiDAR data. The unshaded regions represent added polylines that were copied and their x-coordinates shifted from one of the polylines that represents the observed features, to provide more complete coverage over the area of interest.	3.3
Figure 3.2.	Locations of boreholes or wells where grain-size distribution data were available that were used for hard data (HD) in MPS simulations. The black lines show the outlines of the 200 West and 200 East Areas.....	3.4

Figure 3.3. Profiles of grain-size distribution metrics for two wells. Sediment samples with ratios $dg/sg \geq 1$ were categorized as paleochannel sediments and used as hard data in the MPS simulations. 3.5

Figure 3.4. ERT results from resistivity surveys performed between the 200 West and 200 East Areas (Robinson et al., 2022). Images arranged from northwest (top) to southeast (bottom). Regions shown in red ($EC \leq 0.001$ S/m) were assumed to be more likely to consist of coarser sediments associated with paleochannel features. 3.7

Figure 3.5. Location map showing area of ERT Campaign 1 where the ERT data used in this report came from (from Robinson et al., 2022). 3.8

Figure 3.6. Bulk electrical conductivity (EC) measured in laboratory column experiments with water-saturated, repacked sediment mixtures with different grain-size distributions. The horizontal green dashed line represents a bulk EC value of 0.001 S/m that was used to differentiate between coarser (paleochannel) sediments and finer (non-paleochannel) sediments for soft data (SD). The dashed curves represent fits of linear and non-linear models to the data. Extrapolation of the linear model to the assumed threshold value of EC yields a value of $dg/sg = \sim 1$, which was used in this study to differentiate coarser (paleochannel) and finer (non-paleochannel) sediments for hard data (HD). For Information Only. 3.9

Figure 3.7. Test problem with a three-layer-thick paleochannel feature in the training image (TI), and hard data (HD) and soft data (SD) arranged in patterns that mimic the setup used for MPS simulations in this study. For the TI and HD images, red blocks have index 1 and blue blocks have index 0. The HD data would be analogous to data from 10 wells, 5 of which intersected the paleochannel, and 5 of which did not. Green blocks in the HD image have no value assigned in the actual MPS data file. For the SD, different probabilities were assigned to the vertical slices, ranging from 0.99 to 0.1, with larger values assigned to grid blocks that are closer to the paleochannel feature in the corresponding TI. Blue blocks in the SD image have no values assigned to them in the actual MPS data file. The E-type (expected values) estimate represents the average of 100 realizations. The E-type estimate, as well as individual realizations, reproduce the general shapes of features in the TI and preserve hard data at their measurement locations. 3.10

Figure 3.8. Oblique view from the southwest of the eSTOMP model domain with the zoomed-in portion showing the spatial discretization. The rock/soil types are from top to bottom, the Hanford formation (Hf), the Cold-Creek unit (CCu), the Ringold Taylor flats unit (Rtf), the Ringold E unit (Rwie), the Ringold lower mud (Rlm), and the Ringold unit A (Rwia). Map views of the same model domain are shown in subsequent figures. 3.11

Figure 3.9. Spatial distribution of material types in the base case model at 120-m and 110-m elevations. PC = paleochannels (absent in base case)..... 3.13

Figure 3.10. Spatial distributions of material types based on alternative model realization 0 at 120-m and 110-m elevations. PC = paleochannels. 3.14

Figure 3.11. Spatial distributions of material types based on MPSLib realization 4 at 120-m and 110-m elevations. 3.15

Figure 3.12. Permeability distributions at the 120 m (top) and 110 m (bot) elevations for the base model. 3.17

Figure 3.13. Permeability distributions at the 120-m and 110-m elevations for alternative model realization 0..... 3.18

Figure 3.14.	Permeability distributions at the 120-m and 110-m elevations for alternative model realization 4.....	3.19
Figure 4.1.	Simulated tritium distributions from the base case model at the 120-m elevation for years 1993 and 2047.....	4.2
Figure 4.2.	Simulated tritium distributions from alternative model realization 0 at the 120-m elevation for years 1993 and 2047.....	4.3
Figure 4.3.	Simulated tritium distributions from alternative model realization 4 at the 120-m elevation for years 1993 and 2047.....	4.4
Figure 4.4.	Simulated carbon tetrachloride concentrations from the base model at the 120-m elevation for years 1993 and 2200.....	4.5
Figure 4.5.	Simulated carbon tetrachloride concentrations from alternative model realization 0 at the 120-m elevation for years 1993 and 2200.....	4.6
Figure 4.6.	Simulated carbon tetrachloride concentrations from alternative model realization 4 at the 120-m elevation for years 1993 and 2200.....	4.7
Figure 4.7.	Zoomed-in views of simulated carbon tetrachloride plumes in the year 2200 for the base model (top), alternative model realization 0 (middle), and alternative model realization 4 (bottom).....	4.8
Figure 4.8.	Locations of three separate iodine-129 plumes on the Hanford Site in 1993.....	4.9
Figure 4.9.	Simulated iodine-129 concentrations for the base model at the 120-m elevation for years 1993 and 2200.....	4.10
Figure 4.10.	Simulated iodine-129 concentrations for alternative model realization 0 at the 120-m elevation for years 1993 and 2200.....	4.11
Figure 4.11.	Simulated iodine-129 concentrations for alternative model realization 4 at the 120-m elevation for years 1993 and 2200.....	4.12
Figure 4.12.	Zoomed-in views of simulated iodine-129 plumes in the year 2200 for the base model (top), alternative model realization 0 (middle), and alternative model realization 4 (bottom).....	4.13
Figure 4.13.	Calculated locations of the centers of mass (x_c , y_c) for the simulated carbon tetrachloride (top) and iodine-129 (bottom) plumes between year 1993 and 2500. In the figure legend, <i>basecase</i> refers to the base reference case model results and <i>mps0</i> , <i>mps1</i> , <i>mps2</i> , <i>mps3</i> , and <i>mps4</i> refer to results from alternative model realizations.....	4.15

Tables

Table 3.1.	Half-lives and K_d values used for modeling selected contaminants of concern.	3.16
------------	--	------

1.0 Introduction

Conceptual site models (CSMs) are iterative, “living representations” of contaminated sites. This perspective stems from the need to periodically reassess and update CSMs as new site characterization and monitoring data become available. Information on the features, events, and processes at a site are integrated into CSMs (BHI, 2001; Last et al., 2004). Associated conceptual-mathematical models, implemented with flow and transport simulators, are used as platforms for integrating information about historical events that resulted in subsurface contamination, site characterization data, and operational information associated with cleanup activities. Modeling can be used to enhance our understanding of key processes, evaluate “what-if” questions, optimize operational parameters for remediation activities, assess and mitigate potential future risks, and generally support site decision-making. Understanding the potential impacts of uncertainties associated with CSMs on cleanup actions is critical to ensure appropriate planning and remedy decisions. Evaluating the effects of these uncertainties can ultimately result in better site characterization, monitoring, and remedial decisions.

To this end, the objectives of this report were to develop a methodology for producing alternative CSMs and to demonstrate its applicability to the Hanford Site Central Plateau. The developed methodology accommodates multiple data types, including historical site characterization data and new data obtained using surface geophysical methods that have not been available previously for CSM development at Hanford. Methods such as the one described here are needed to allow for the systematic use of these new geophysical data sets, together with more traditional data. The developed methodology was used to generate multiple realizations of alternative models that contain paleochannel features. Such features may be preferential flow paths for contaminants of concern (COCs). The alternative models allow for assessment of the effects of potential uncertainties in paleochannel features on water flow and contaminant transport behavior.

This report describes the use of a multipoint geostatistics (MPS) framework that can use multiple data types for developing alternative conceptual-mathematical models of the subsurface at Hanford. This effort represents the first time MPS have been applied in the development of subsurface flow and transport models for the Hanford Site. The multiple data types that were used in this study include grain-size distribution, electrical resistivity tomography (ERT), and Light Detection and Ranging (LiDAR)-based digital elevation data of ground surface topography.

The LiDAR data show outlines of relic paleochannel features that were formed by the ancestral Columbia River and flooding events in the past. These relic paleochannel features are assumed to be representative of similar paleochannel features that exist in the subsurface and influence water flow and contaminant transport behavior. The LiDAR-based elevation data were used to develop a training image (TI) for the MPS algorithm. Profiles of grain-size distribution metrics from sediment samples collected during drilling of boreholes and wells show regions of very coarse, well-sorted sediments that were assumed to be indicative of paleochannel features. Images of ERT data also show regions of very low electrical conductivity (EC) that resemble cross-sections through channels. Therefore, binned grain-size distribution metrics from selected borehole samples, and ERT data from selected measurement transects, were also used, as hard (known) and soft (uncertain) categorical data, respectively, for identifying paleochannel features with the MPS algorithm.

The alternative conceptual models were implemented numerically using the subsurface flow and transport simulator eSTOMP (Fang et al., 2018; <https://www.pnnl.gov/estomp>). Simulations of the transport of three COCs – tritium, carbon tetrachloride, and iodine-129 – were performed using the alternative conceptual models and a base or reference case that was developed from the Plateau-to-River (P2R) model of the Hanford Site (Budge, 2020). Model results illustrate some of the potential effects of

uncertainties in paleochannel features on predicted transport and fate of selected COCs at Hanford. Some limitations of the approach and data needs are also discussed.

The report is organized as follows. Section 2.0 provides background on site characterization at Hanford. Section 3.0 describes the methods and the different types of data that were used in this study. Section 4.0 presents transport simulation results for a base or reference model and five realizations of alternative conceptual models for three COCs – tritium, carbon tetrachloride, and iodine-129. A summary of the work and conclusions are provided in Section 5.0, followed by a description of the quality assurance procedures applied to study (Section 6.0) and the references (Section 7.0).

2.0 Background

A variety of data types are collected at the Hanford Site for site characterization. Such data may include grain-size distribution and chemical analysis data from core and grab samples, vadose zone hydraulic properties determined on both intact and repacked core samples, borehole geophysical logs, and aquifer tests performed over screened intervals in wells (Serne et al., 2010; Rockhold et al., 2018). Until relatively recently, the majority of site characterization information was based on data collected from samples obtained by well drilling. Borehole- and well-based data provide “ground truth” information needed for most site characterization and model parameterization efforts.

Although thousands of boreholes and wells have been drilled, the Hanford Site covers an area of 586 mi², so well coverage is relatively sparse compared to the scales of hydrogeologic features that control subsurface flow and transport. The elevations of interfaces between major hydrostratigraphic units have been interpreted from drilling records and from core and borehole geophysical log data. These elevations, a.k.a. “picks” or “tops,” have been interpolated between borehole and well locations to create surfaces that are combined to build geologic framework models (GFMs) for the site (Hammond, 2015). GFMs, which are essentially simplified, layered representations of the subsurface, have been developed to support both Hanford site-wide modeling efforts (Budge, 2020) as well as area- or operable unit-specific modeling activities (Rockhold et al., 2019). Sparsity of boreholes and wells can result in significant uncertainty about the presence or absence, and dimensions or configuration, of subsurface features. For example, features such as paleochannels, which may be preferential flow paths for COCs, can appear to be discontinuous or even absent across larger areas of interest, owing to sparse well coverage.

Surface-based geophysical methods such as ERT, electromagnetics, and seismic reflection/refraction data have been collected recently at Hanford (Robinson et al., 2022). The use of surface-based geophysical methods for augmenting borehole-based site characterization and monitoring is attractive owing to the ability of these methods to provide spatially extensive 2-D and 3-D information in areas with limited or no well coverage. ERT can also provide near real-time data acquisition and processing, which can be very useful for monitoring field remediation activities (e.g., soil flushing). One challenge with using surface-based geophysical methods is that they are sensitive to multiple variables. For example, bulk resistivity measurements (or their inverse, bulk EC), which are used for ERT, are sensitive to porosity, water saturation, ionic strength of the pore water, clay content, and temperature. If most of these variables are either known, or static (not changing in time), repeat or time-lapse surveys can be used as straightforward change-detection techniques for variables that are known to be changing. For example, Robinson et al. (2019) performed numerical experiments that demonstrated the feasibility of using ERT to track the movement of a nitrate plume in groundwater located ~60 m below ground surface in the Hanford 200 East Area. Quantitative use of surface geophysical data, such as ERT and seismic data, for estimating system properties (e.g., porosity) or system states (e.g., water saturation, solute concentration, matric potential) generally requires the use of correlation functions, or so-called *petrophysical relations*, such as Archie’s law, which relates the bulk EC to the multiple variables that affect it. Supporting data that can be used to define petrophysical relations are typically measured in laboratory studies.

A systematic method is developed and demonstrated in this report for using multiple data types, including ERT, for generating multiple alternative conceptual-mathematical model of the subsurface that include paleochannel features. The ERT data are used in this study as categorical, soft (or uncertain) data in an MPS framework.

3.0 Methods

This section describes a methodology that was developed to generate conditional simulations of paleochannel features that were used in alternative conceptual-mathematical models of subsurface flow and transport. A number of simplifying assumptions were made to provide a clearer description and demonstration of the workflow. Some of these assumptions can be changed, or refined, to produce more detailed representations of subsurface features and properties, as needed.

3.1 Multipoint Geostatistics

This study used an MPS framework for generating conditional simulations of paleochannel features. MPS is a pixel-based geostatistical method for integrating information about the shapes, scales, and connectivity of large-scale features, honoring direct point measurements (or hard data) at their measurement locations, and accounting for other types of information (or soft data) that are uncertain but correlated with the hard data (Strebelle, 2002; Mariethoz et al., 2010; Hansen et al., 2016, 2018). MPS differs from the more traditional two-point covariance (or variogram) function model approach in that it obtains information about spatial structure from TIs. Pattern matching techniques are used to quantify and reproduce patterns of spatial structure and connectivity that are in the TI. MPS is better-suited than variogram-based models for reproducing larger-scale, well-connected features such as braided or meandering stream channels. An interesting recent application of MPS for the joint simulation of redox zones and geological architectures is described by Madsen et al. (2021). The open-source MPS library, MPSLib (Hansen et al., 2018; <https://mpslib.readthedocs.io/en/latest/>), was used in this study to generate multiple realizations of paleochannel features conditioned on both hard and soft data. Details regarding TI development and the hard and soft data used for the MPS simulations are described below.

3.1.1 Training Image

TIs of fluvial features can be generated in different ways, ranging from segmenting (a.k.a. binning) digital data from photographs of outcrops, or segmenting LiDAR-based elevation data (Pirrot et al., 2014), to sampling fluvial features that are generated using other methods (Deutsch and Tran, 2002; Pyrcz et al. 2008). For this study, a TI was generated using LiDAR-based digital elevation data that show relic paleochannel features exposed on the ground surface of the Hanford Site. The LiDAR-based digital elevation data also define the elevation of the ground surface that is used in the Hanford South Geologic Framework Model (Hammond, 2015).

To generate the TI used in this study, a 2D (X-Y) grid was first defined, based on the X-Y cell centroid coordinates of the eSTOMP model grid. Coordinates of polylines were then determined that define the 2D outlines of relic paleochannel features that are visible in the LiDAR-based elevation data (Figure 3.1). The coordinates of one set of polyline points were also copied to produce three additional sets of polylines. The X-coordinates of these polylines were shifted to provide more complete coverage of polylines that define paleochannel features over the area of interest. As shown in Figure 3.1, two of the shifted polylines were placed in the western ~1/3 of the simulation domain, and one was placed near the eastern edge of the domain. The polyline coordinates were used to define cell centroid locations in the 2D grid that were either inside or outside of the polylines. Grid locations inside of polyline coordinates were identified as paleochannel features (index 1) and grid locations outside of polyline coordinates were identified as background material (index 0) for the 2D TI.

Bjornstad (2006) refers to the area where the relic paleochannel features are visible in the LiDAR data as the central Hanford braidplain. He notes that these features were probably formed from the last of the successively smaller Columbia floods at the end of the last glacial cycle around 14,000 to 15,000 years ago. The western part of the model domain is farther away from the Columbia River and does not show the relic paleochannel features that are evident in the LiDAR-based elevation data that are closer to the river. Fecht et al. (2004, 2006) provide interpretations of the sediment sequences and bedforms in the Hanford Reach area. They categorize the central Hanford braidplain as being in the area of *Relief Generation IV*, which they define as Late Pleistocene-age glacial runoff from melting of the continental ice sheet and Holocene-age post glacial mainstream and sidestream alluvium. The area to the west, which includes the Hanford Central Plateau, is categorized as *Relief Generation III*, which they define as Pleistocene-age glacial outburst flood deposits from glacial lake Missoula and other ice-margin lakes. These interpretations suggest that older paleochannel features could be larger and have different orientations than those that are visible in the LiDAR data.

ERT data collected between the 200 West and 200 East Areas provide supporting evidence of apparent north-south trending paleochannel features (Robinson et al., 2019, 2022) within the Relief Generation III area described by Fecht et al. (2006). The ERT data resemble channel cross-sections, but alone the data are insufficient for clearly defining the scales or orientations of the apparent paleochannel features with confidence. However, the available ERT data were used as *soft* (or uncertain) data for the MPS simulations, as described in a subsequent section of this report. Additional ERT and seismic data were collected in fiscal year (FY) 2022 that may provide further evidence for paleochannels (and their dimensions and orientations), as well as additional soft data that can be used in MPS simulations.

For 3D simulations, the TI should contain information about the spatial variability and connectivity of the features of interest in all three principal coordinate directions. The LiDAR-based elevation data can be used to define the detailed 3D morphology of the relic paleochannel features, after defining channel centerlines, perpendicular lines of cross-section at many locations along the lengths of the paleochannels, and the channel shapes for each cross-section. Algorithms were developed for these calculations, but they were not used for the work presented here. Visual inspection of the relic paleochannel features in the LiDAR-based digital elevation data indicate that there are elevation differences of up to ~30 m between the bottoms of the channels and the tops of their banks. The spatial domain of interest is large, but a relatively coarse model grid was used. A much finer grid, and significantly more computational effort, is required to reproduce the full 3D details of the channel morphologies. Therefore, the 2D TI was used as a template, and this template was duplicated twice, and stacked vertically, to generate a 3D (3-layer) TI with 10-m spacing between layers. This simplified approach was found to be adequate for producing simulated paleochannel features that resemble the TI (see Figure 3.7).

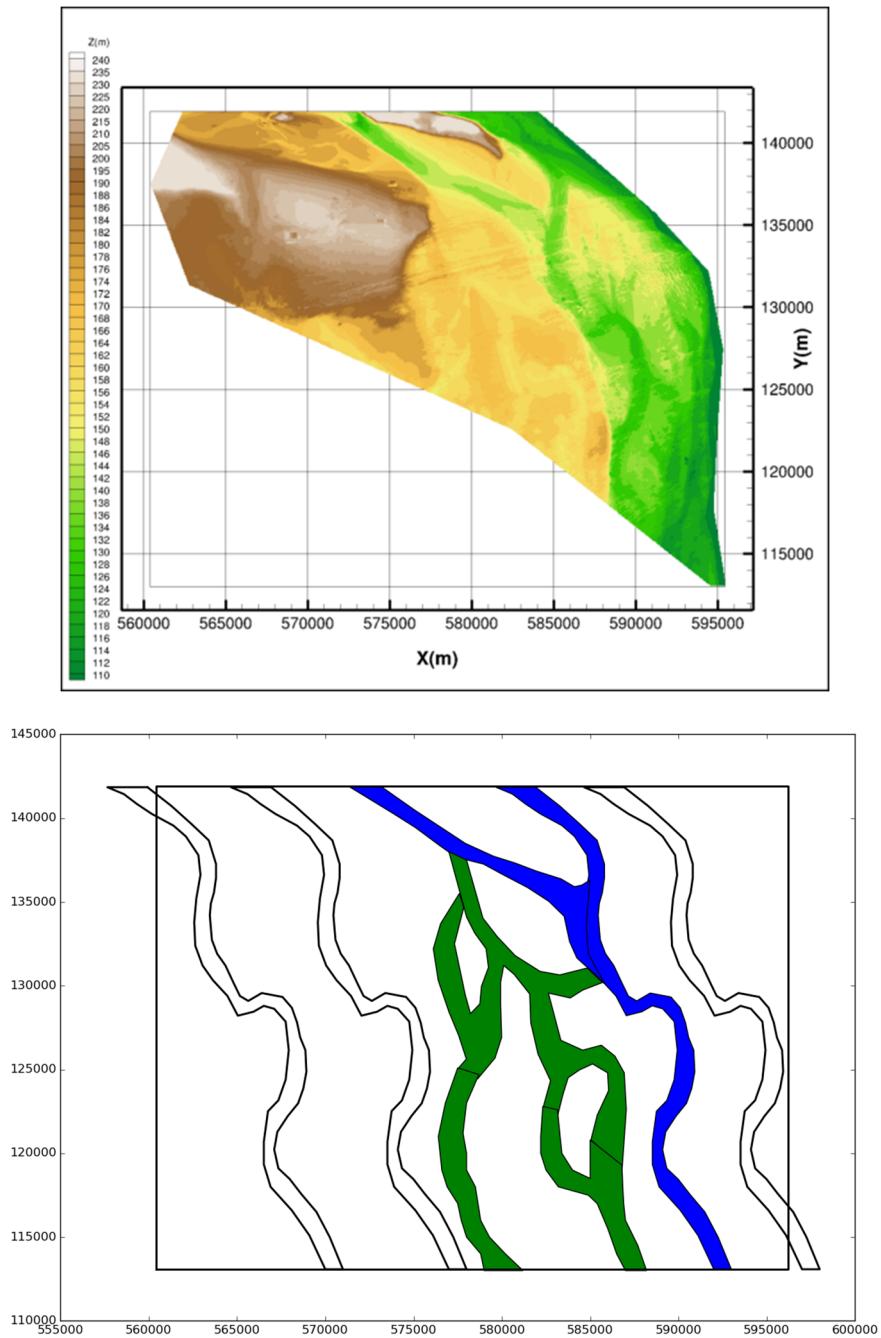


Figure 3.1. LiDAR-based ground surface elevation data (top), and outlines or areas defined by polylines representing relic paleochannel features (bottom). The shaded blue and green regions in the lower plot represent areas where relic paleochannel features are observable in the LiDAR data. The unshaded regions represent added polylines that were copied and their x-coordinates shifted from one of the polylines that represents the observed features, to provide more complete coverage over the area of interest.

3.1.2 Hard Data

Channel-fill materials can contain a wide variety of sediment sizes and typically exhibit fining-upward cycles (Miall 1977, 2014). The coarsest materials, associated with higher-energy flows, are typically located at the base of a channel, or at the bottom of a depositional cycle. Multiple cycles may occur, depending on the nature of the flows, and sediment loads. Cataclysmic flooding events could create a combination of extreme erosion, with partial or complete destruction of existing channels, together with deposition of sediments in the remaining and/or newly-created channels. Given the known correlation between coarser-grained sediments and higher-energy flows, it was assumed that paleochannel fill material would generally be coarser than surrounding materials (e.g., overbank flood and crevasse splay deposits).

Grain size distribution metrics for 2575 sediment samples collected from 50 boreholes and wells on the Central Plateau were analyzed and binned into classes (Figure 3.2). In plan view, almost all of the well or borehole locations shown in Figure 3.2 are within the area that is designated as the high-conductivity zone (HCZ) in the P2R model (Budge, 2020; see red and orange colored area of higher permeabilities in Figure 3.13). Well locations were selected based on proximity to areas of interest where ERT surveys were being conducted or planned, and based on the availability of data in the ROCSAN database. The sediment grain size distribution metrics were determined using sieve data downloaded from the Hanford Virtual Library.¹ The selected sediment samples are assumed to be generally representative of sediments that exist in the subsurface underlying the Central Plateau, but the numbers of samples representing particular hydrostratigraphic units were not determined. Also, as shown in Figure 3.2, relatively few data were available for the 200 West Area.

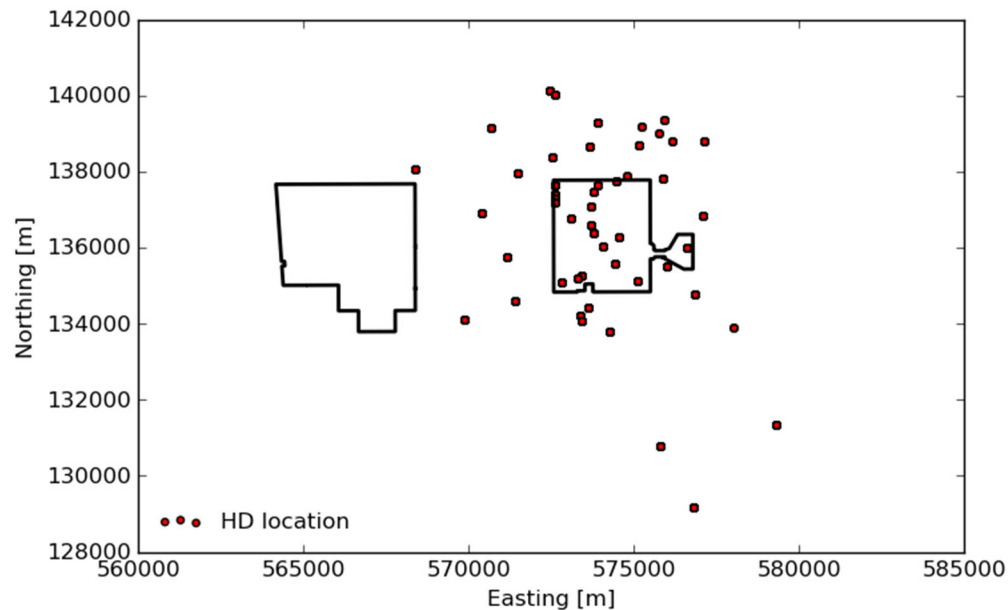


Figure 3.2. Locations of boreholes or wells where grain-size distribution data were available that were used for hard data (HD) in MPS simulations. The black lines show the outlines of the 200 West and 200 East Areas.

¹ <http://vlprod.ri.gov/vlib/app/index.cfm?TID=F70AD85EEA91737160C39F08DAF572363A27DDF61BA2833010E967323567409B>

Figure 3.3 shows profiles of the geometric mean grain diameter, d_g , geometric standard deviation, s_g , and their ratio, d_g/s_g , that were computed for the sieve data from two wells. The d_g/s_g metric is a ratio of size and sorting metrics. The plots for these two wells both show a region between about the 110- and 140-m elevations with $d_g/s_g \geq 1.0$, which is indicative of very coarse, well-sorted sediments. For the purposes of this study, locations with d_g/s_g values ≥ 1.0 were categorized as paleochannel sediments and were used as hard (known) data for MPS simulations. It is recognized that this is a simplification and paleochannel fill materials are more likely to consist of “packages” of sediment that contain a range of different sediment sizes/classes. The maximum grain size that can be transported is also a function of flow velocity, so flood events of different magnitudes would transport sediments of different sizes classes. Nevertheless, the threshold $d_g/s_g \geq 1.0$ was used here for demonstration purposes. Additional details are provided in Section 3.1.3.

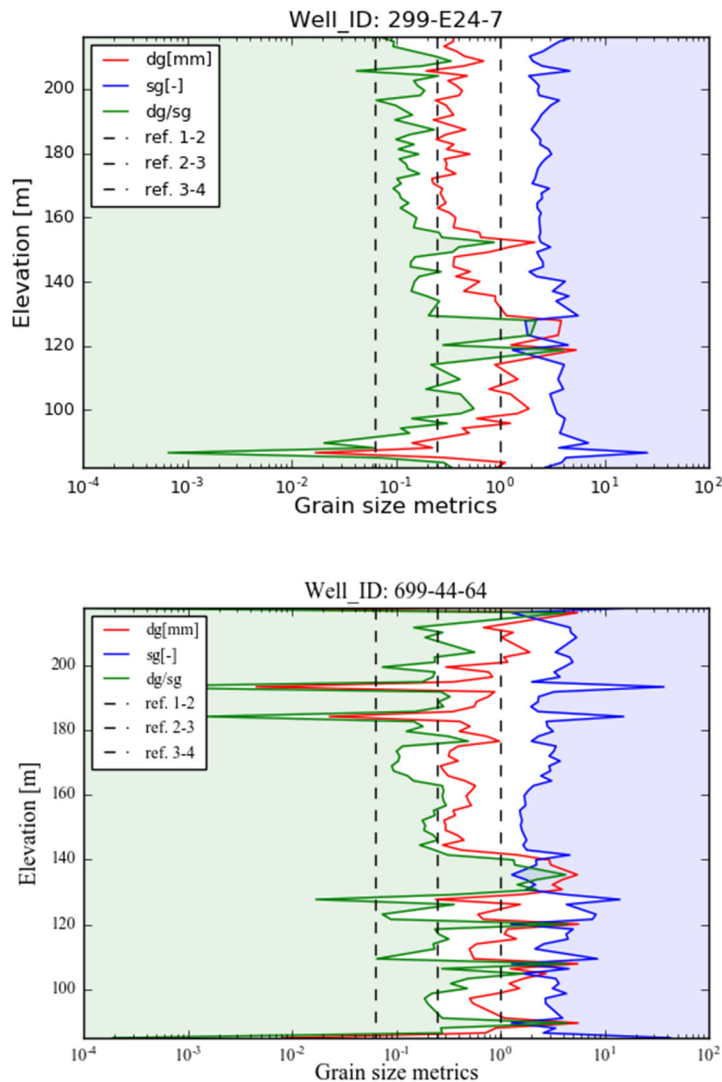


Figure 3.3. Profiles of grain-size distribution metrics for two wells. Sediment samples with ratios $d_g/s_g \geq 1$ were categorized as paleochannel sediments and used as hard data in the MPS simulations.

3.1.3 Soft Data

Figure 3.4 shows bulk EC values produced by ERT for selected resistivity surveys that were performed between the 200 East and 200 West Areas (Robinson et al., 2022). These data represent five of the parallel survey lines from the area labeled as *ERT Campaign 1* shown in Figure 3.5 (Robinson et al., 2022). The EC values from these survey lines were sampled and binned to identify regions with coarser sediments that are more likely to be associated with paleochannels. For water-saturated sediments, EC values < 0.001 S/m were assumed to be indicative of coarser sediments that have a higher likelihood of being located in paleochannels. These regions are shown in red in Figure 3.4. The selection of this threshold is based primarily on the similarity of shapes and sizes of the apparent channel features that appear when this threshold is used, relative to expectations for channels shapes and sizes in this area. This threshold is also supported by a limited set of laboratory experimental data.

Figure 3.6 shows bulk EC data that were measured in laboratory column experiments for three different mixtures of water-saturated, repacked Hanford sediments. Synthetic groundwater was used in the experiments. The sediment mixtures were sieved and recombined to achieve different values of d_g/s_g . The trend of the data shows that bulk EC decreases with increasing values of d_g/s_g . Extrapolation of the linear fit to the data suggests that for water saturated sediments, bulk EC values < 0.001 S/m correspond approximately with values of $d_g/s_g > 0.95$ (~ 1.0). Extrapolation of the non-linear fit suggests that values of EC < 0.001 S/m correspond approximately to values of $d_g/s_g > 0.57$ (~ 0.6). These relationships provide a range for potential threshold values of d_g/s_g for an associated bulk EC that could be used to differentiate paleochannel and non-paleochannel sediments. However, additional data are clearly needed to corroborate or refine these relationships. Hanford formation sediments are unconsolidated but Ringold Formation sediments may be semi-consolidated, so different petrophysical relations may apply to those sediments.

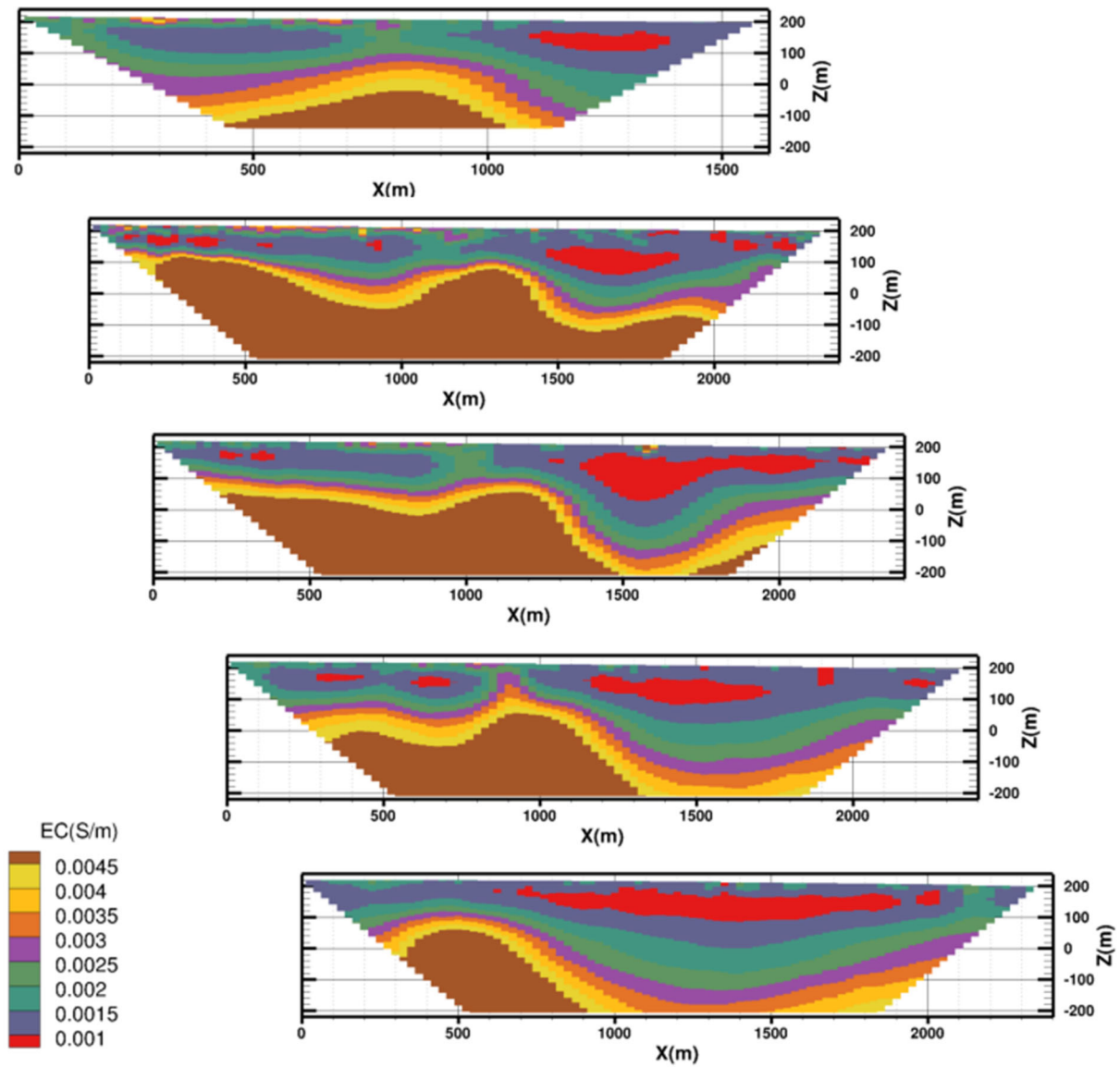


Figure 3.4. ERT results from resistivity surveys performed between the 200 West and 200 East Areas (Robinson et al., 2022). Images arranged from northwest (top) to southeast (bottom). Regions shown in red ($EC \leq 0.001$ S/m) were assumed to be more likely to consist of coarser sediments associated with paleochannel features.

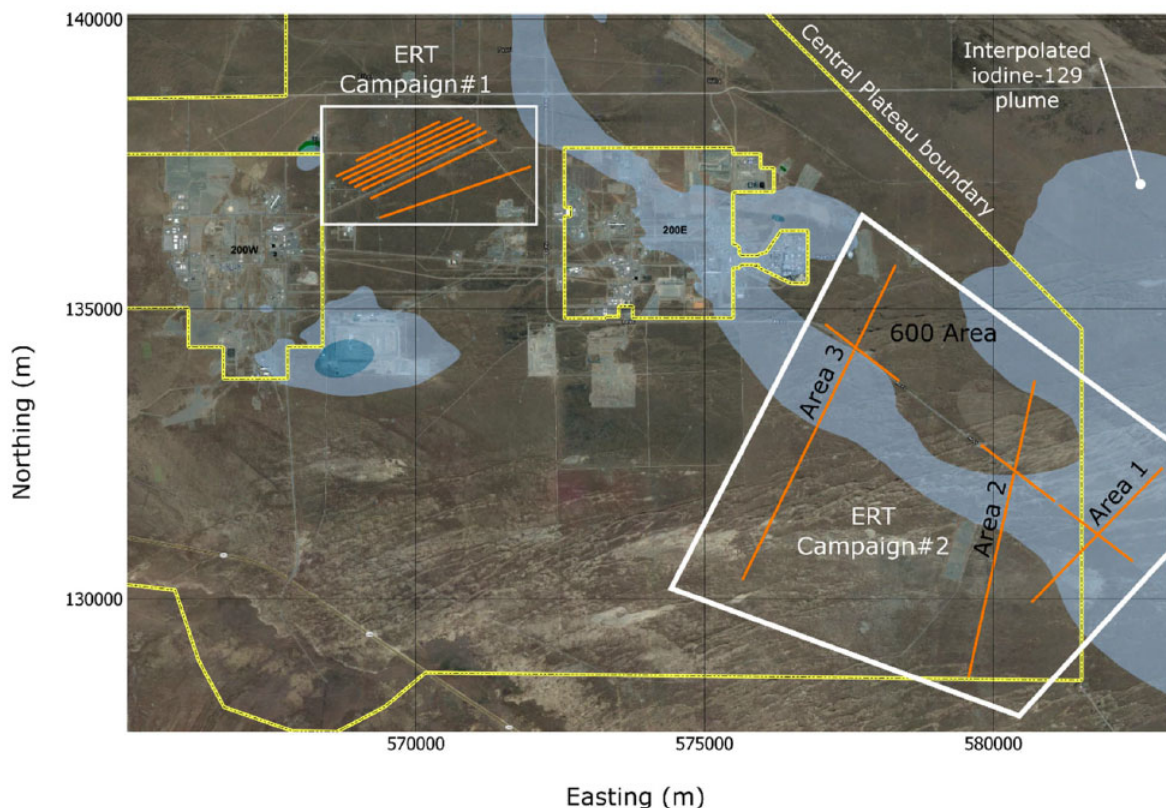


Figure 3.5. Location map showing area of ERT Campaign 1 where the ERT data used in this report came from (from Robinson et al., 2022).

Sampled locations with $EC < 0.001$ S/m were assigned a probability of 0.9 of being in a paleochannel, and a probability of 0.1 of being background material. Sampled locations with $EC \geq 0.001$ S/m were assigned a probability of 0.9 of being background material, and probability of 0.1 of being paleochannel sediment. These assigned probabilities are somewhat arbitrary but were selected so that locations with very low EC values would be more likely to have a paleochannel feature generated in that location of the model grid by the MPS algorithm.

Probabilities assigned to soft (uncertain) data would normally be calculated directly, for example, by simply counting the number of occurrences of EC values < 0.001 S/m for locations that are known to be very coarse sediments (that are likely to be high-energy paleochannel deposits), relative to the total number of EC values in a data set. However, another challenge with using ERT at Hanford is that groundwater monitoring wells are completed with steel casing that generally interferes with the electrical resistivity measurements that are made in their vicinity. Therefore, it is difficult to find ground truth data from wells that can be directly paired with ERT data, unless the resistivity surveys are performed before, rather than after, a well is drilled. This problem can only be resolved by careful planning to ensure that at least some resistivity surveys are performed along lines that intersect the locations of planned characterization wells, prior to drilling the wells. If this is done, bulk EC data from ERT could be directly compared to sample-based textural classifications, porosity, saturations, etc., and probabilities assigned to ERT data that are used as soft data in MPS simulations could also be easily generated. This sequencing could also provide field-based petrophysical data that would likely be superior to laboratory petrophysical data. Another option would be to use different casing materials that are non-conductive, such as polyvinyl chloride.

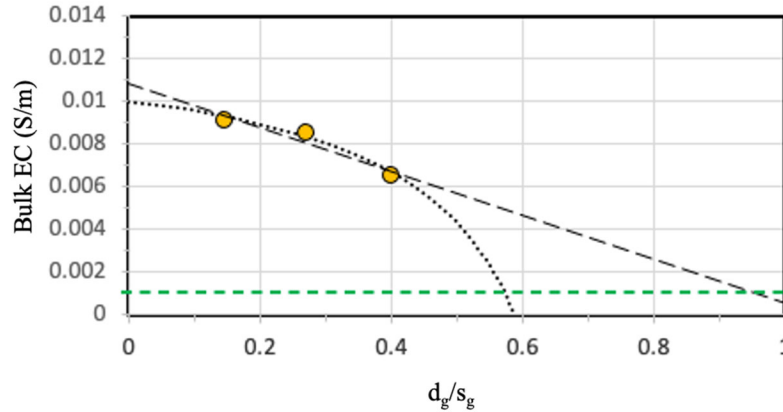


Figure 3.6. Bulk electrical conductivity (EC) measured in laboratory column experiments with water-saturated, repacked sediment mixtures with different grain-size distributions. The horizontal green dashed line represents a bulk EC value of 0.001 S/m that was used to differentiate between coarser (paleochannel) sediments and finer (non-paleochannel) sediments for soft data (SD). The dashed curves represent fits of linear and non-linear models to the data. Extrapolation of the linear model to the assumed threshold value of EC yields a value of $d_g/s_g = \sim 1$, which was used in this study to differentiate coarser (paleochannel) and finer (non-paleochannel) sediments for hard data (HD). For Information Only.

Figure 3.7 shows the results from a test problem in which a TI with three layers representing a paleochannel feature was used together with both hard and soft data. The configuration of the hard and soft data in the test problem mimics the orientations of well-based data and ERT data, respectively, and how they were used in this study. Simulation results for E-type (average or expected value) estimates, as well as individual realizations, reproduce the general shapes of features in the TI and preserve the hard data at their measurement locations.

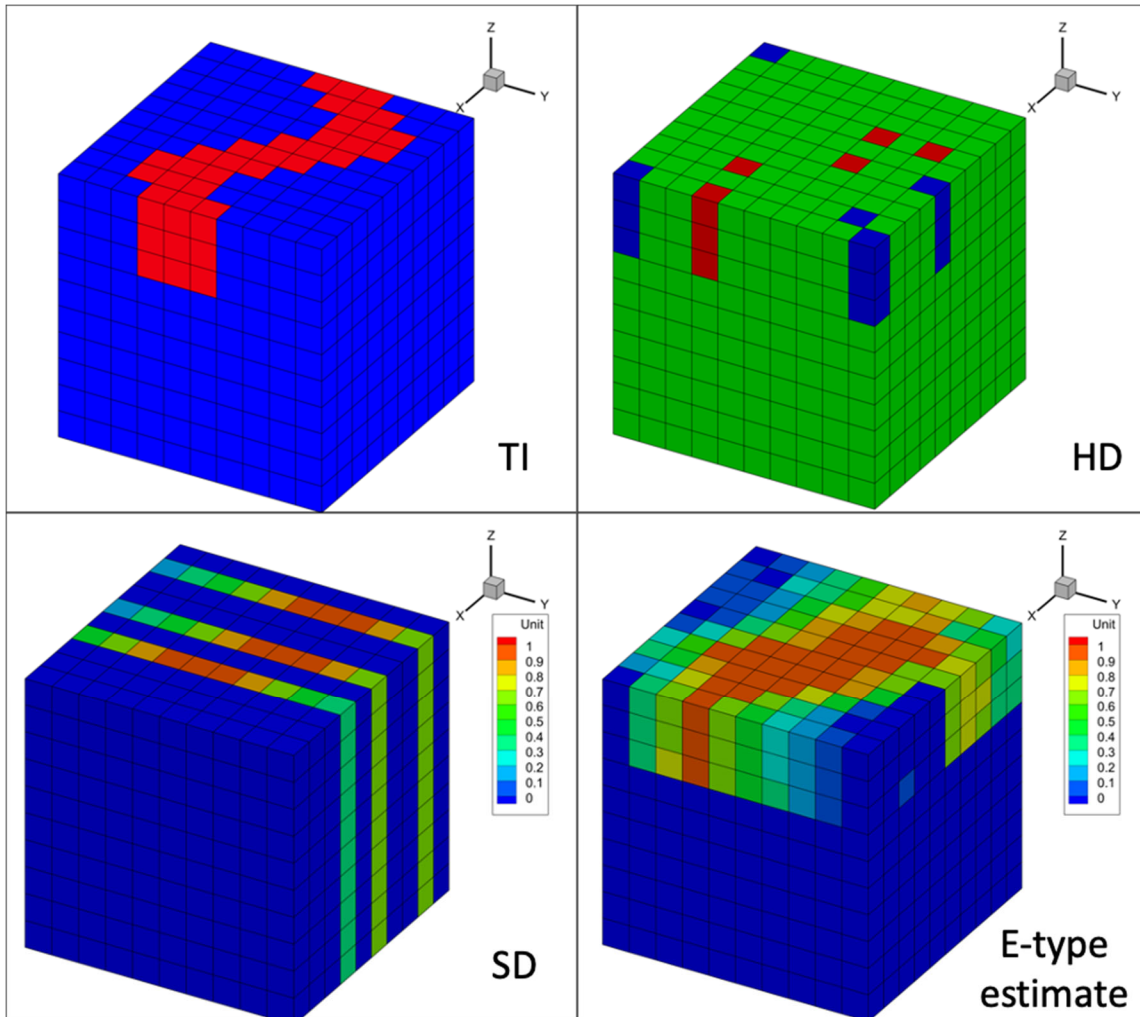


Figure 3.7. Test problem with a three-layer-thick paleochannel feature in the training image (TI), and hard data (HD) and soft data (SD) arranged in patterns that mimic the setup used for MPS simulations in this study. For the TI and HD images, red blocks have index 1 and blue blocks have index 0. The HD data would be analogous to data from 10 wells, 5 of which intersected the paleochannel, and 5 of which did not. Green blocks in the HD image have no value assigned in the actual MPS data file. For the SD, different probabilities were assigned to the vertical slices, ranging from 0.99 to 0.1, with larger values assigned to grid blocks that are closer to the paleochannel feature in the corresponding TI. Blue blocks in the SD image have no values assigned to them in the actual MPS data file. The E-type (expected values) estimate represents the average of 100 realizations. The E-type estimate, as well as individual realizations, reproduce the general shapes of features in the TI and preserve hard data at their measurement locations.

3.2 Flow and Transport Models

3.2.1 Grid

A reference or base case subsurface flow and transport model of the portion of the Hanford Site south of Gable Mountain and Gable Butte was developed using eSTOMP. The model was based on the Hanford South GFM (Hammond, 2018) and the calibrated MODFLOW- and MT3D-based P2R model (Budge, 2020). Like the P2R model, the reference eSTOMP model is bounded on the top and bottom by the ground surface and the top of basalt, respectively, and uses a boundary-fitted grid that conforms with those upper and lower bounding surfaces.

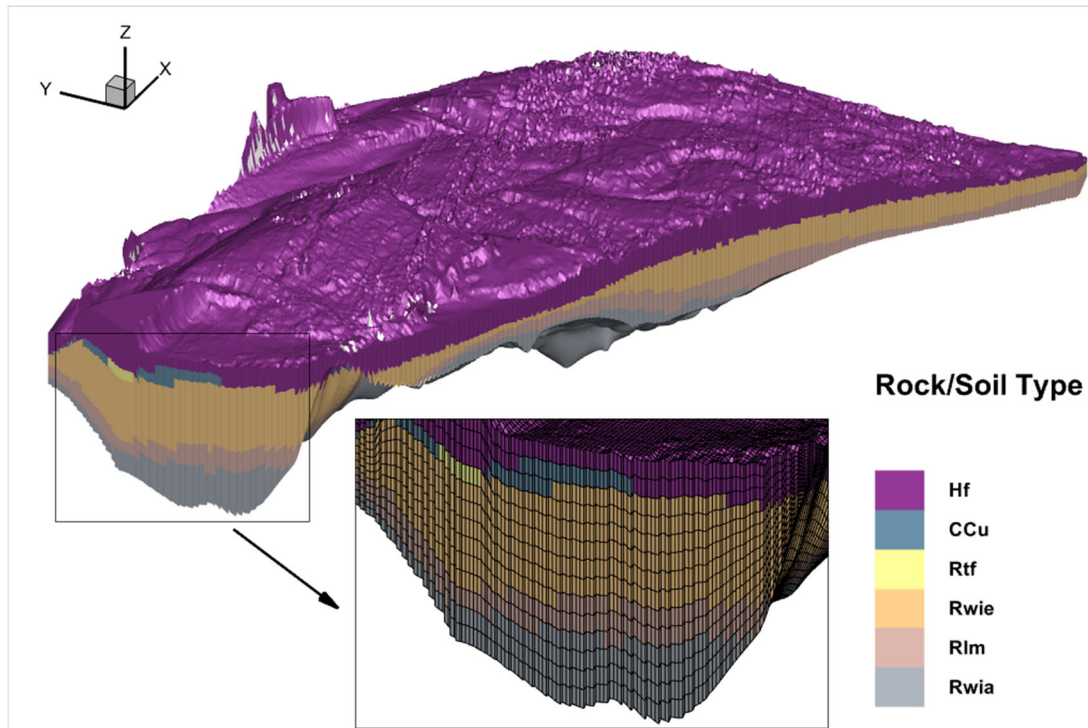


Figure 3.8. Oblique view from the southwest of the eSTOMP model domain with the zoomed-in portion showing the spatial discretization. The rock/soil types are from top to bottom, the Hanford formation (Hf), the Cold-Creek unit (CCu), the Ringold Taylor flats unit (Rtf), the Ringold E unit (Rwie), the Ringold lower mud (Rlm), and the Ringold unit A (Rwia). Map views of the same model domain are shown in subsequent figures.

However, for the eSTOMP model, the vertical extent of the model domain was subdivided into 14 layers (Figure 3.8), rather than the 7 layers used by the P2R model. At any given x-y location in the reference model, each of the 14 layers has equal thickness. More layers were used in the eSTOMP model to obtain more favorable aspect ratios for some portions of the model domain, and because eSTOMP uses parallel processing, so run times were not a concern. The Hanford South GFM was used to assign a material type designation to each grid block in the active eSTOMP model domain.

The eSTOMP model is discretized using 350, 289, and 14 grid blocks in the x-, y-, and z-directions, respectively, for a total of 1,416,100 grid blocks. Grid blocks located in some portions of the domain are inactive (e.g., in area southwest of Washington State Route 240, and within the area of the active flow channel of the Columbia River). In the easting and northing directions, the eSTOMP model spans a distance of 35 km (easting coordinates 595,400 to 560,400 m) and 28.9 km (northing coordinates 141,900

to 113,000 m), respectively. Uniform, 100-m grid spacing was used in the horizontal directions. In contrast, the P2R model uses either 100-m or 200-m grid spacing in the horizontal directions, with 100-m resolution used in the area of the Central Plateau and 200-m resolution used elsewhere (Budge, 2020).

3.2.2 Material Type Distributions

Figure 3.9, Figure 3.10, and Figure 3.11 show plan views of the material types in the base model and in two alternative model realizations containing paleochannel features, for horizontal slices through the model domains at the 120-m and 110-m elevations. With the exception of the paleochannel material, all other materials are based on the major hydrostratigraphic units in the Hanford South GFM (Hammond, 2018). These consist, from top to bottom, of the Hanford formation (Hf), the Cold Creek unit (CCu), the Ringold Taylor flats unit (Rtf), the Ringold unit E (Rwie), the Ringold lower mud (Rlm), and the Ringold unit A (Rwia).

The alternative conceptual-mathematical models containing paleochannel features were generated using the *genesim* algorithm from the multipoint simulation library, MPSLib (Hansen et al., 2016; <https://mpslib.readthedocs.io/en/latest/>). MPSLib was used to generate categorical data representing different realizations of paleochannel features embedded within a background material. For this study, the TI and the binned grain-size distribution and ERT data that were used as hard and soft data, respectively, were used to generate five realizations of paleochannel features that were superimposed on the zonation file that was used for the base case model. Any number of realizations can be generated by MPSLib, and each realization is different, but each one contains features that resemble the TI and preserves the hard data at their measurement locations. The probabilities of certain material types appearing in certain locations are also affected by the soft data.

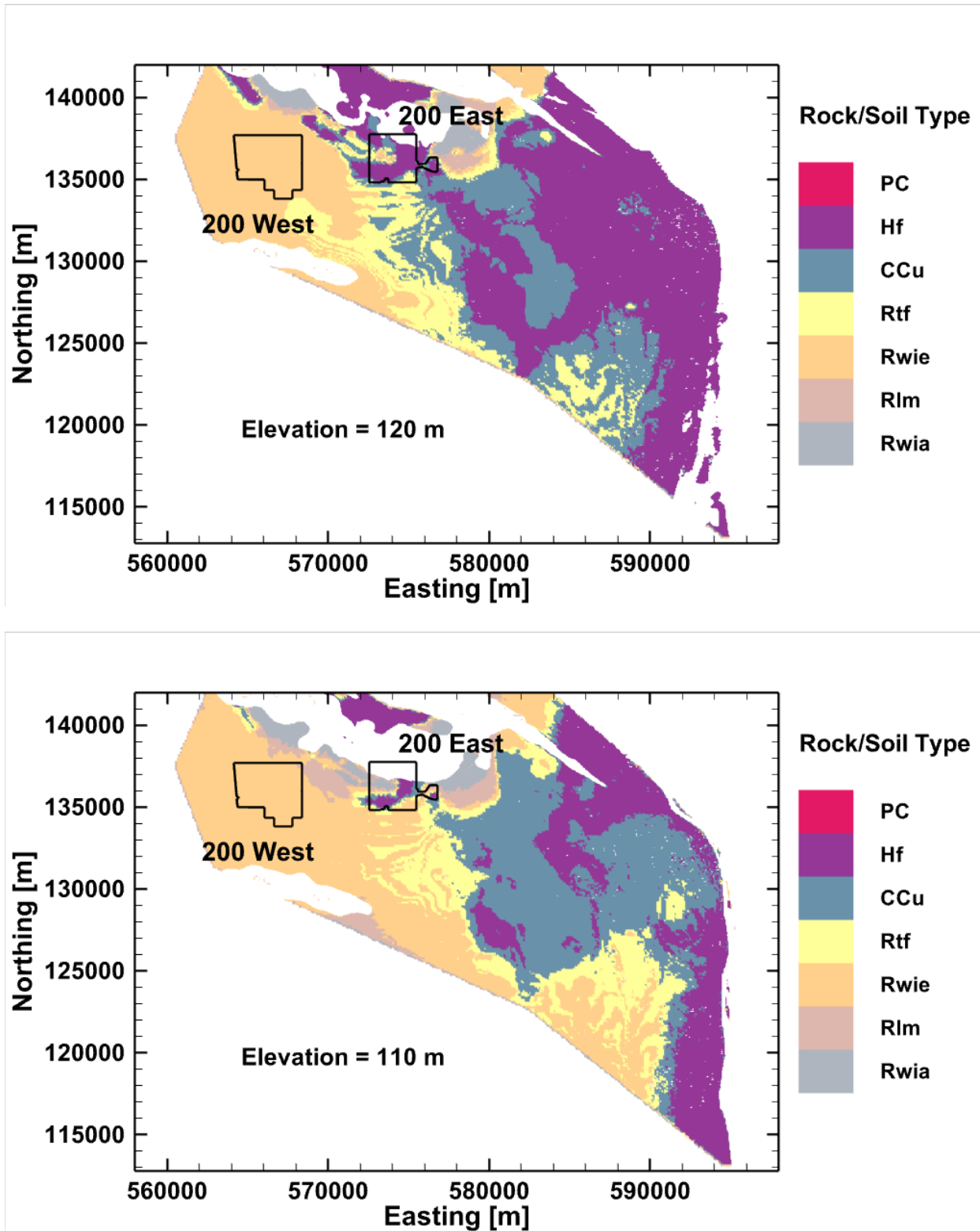


Figure 3.9. Spatial distribution of material types in the base case model at 120-m and 110-m elevations. PC = paleochannels (absent in base case).

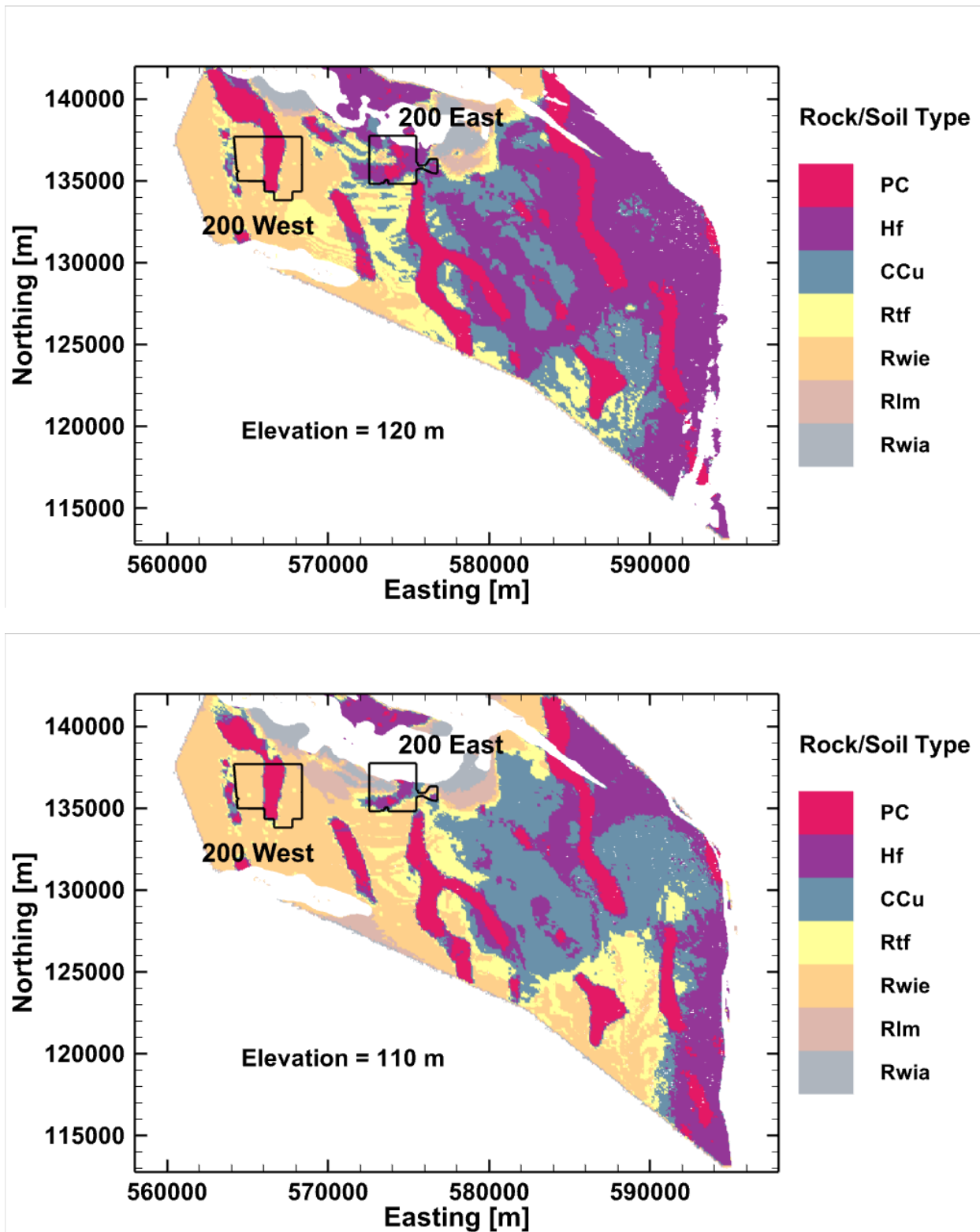


Figure 3.10. Spatial distributions of material types based on alternative model realization 0 at 120-m and 110-m elevations. PC = paleochannels.

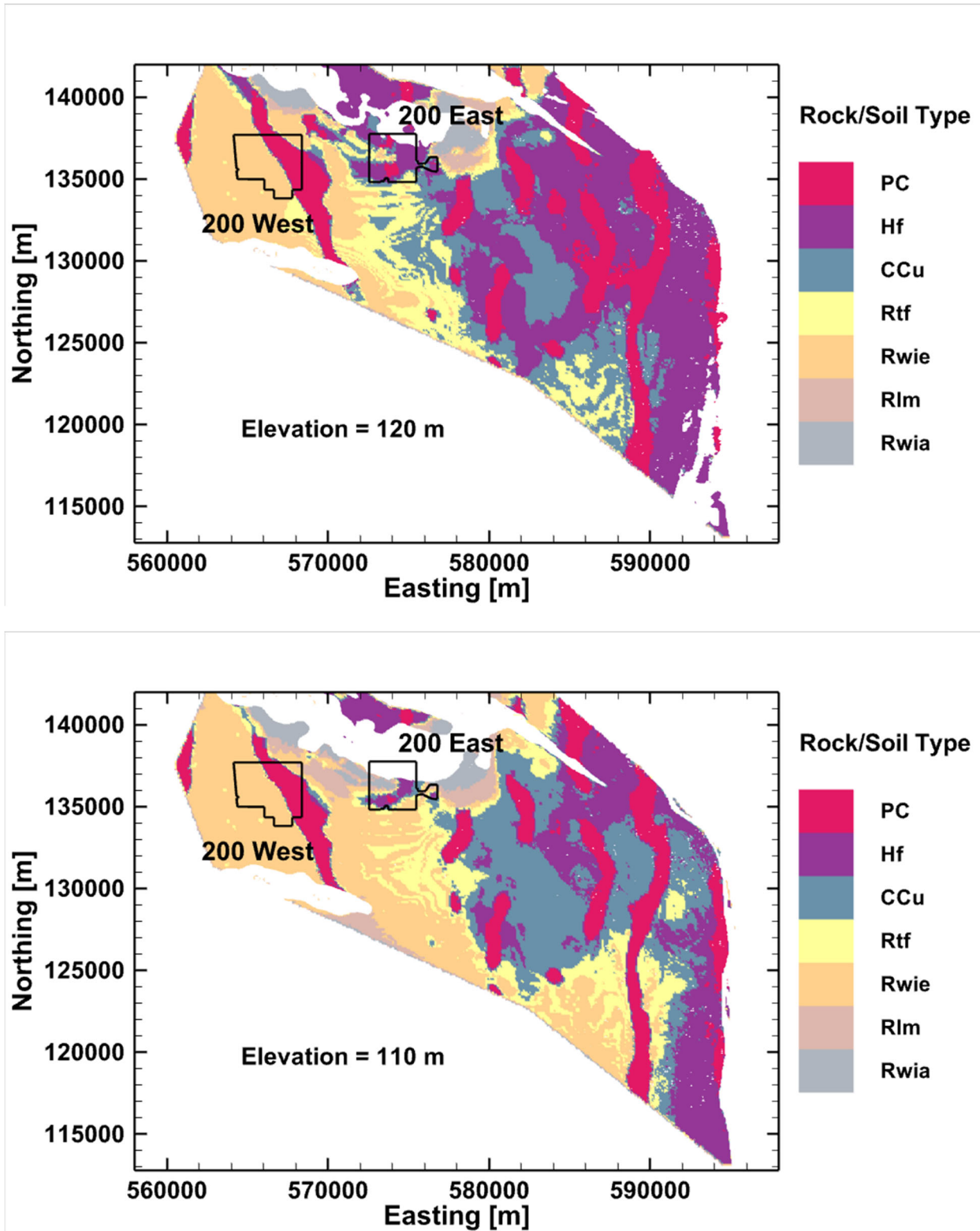


Figure 3.11. Spatial distributions of material types based on MPSLib realization 4 at 120-m and 110-m elevations.

3.2.3 Material Properties

Spatially variable permeability values were used in the reference eSTOMP model based on permeability values from the calibrated MODFLOW-based P2R model. Since the P2R and eSTOMP models use different grids, the permeability values used in the reference eSTOMP model were based on a nearest neighbor property assignment from the P2R model grid. Figure 3.12 shows the distribution of permeability values used in the base eSTOMP model at the 120- and 110-m elevations. The large northwest-to-southeast trending region of higher permeabilities (shown red and orange in Figure 3.12) that runs through the 200 East Area is the area known as the HCZ in the P2R model (Budge, 2020). A constant value of 0.15 was used for porosity for consistency with what was used in MT3D simulations with the P2R model (personal communication with Trevor Budge, INTERA).

For the alternative models, the permeability values used for model grid blocks that were flagged as paleochannel features were scaled up by a factor of 1.5, relative to the values used in the base model. This approach was used to provide a simple method for illustrating how discrete paleochannel features with higher permeability might affect transport results relative to the base or reference case. The generated paleochannel features are smaller than the HCZ, but are superimposed on it and elsewhere within the model domain. Figure 3.13 and Figure 3.14 show the distribution of permeability values used in two of the alternative model realizations at the 120 and 110 m elevations. Differences between the permeability fields for the alternative realizations and the base model are subtle on the log scale plots. A constant porosity value of 0.15 was also used for the alternative models.

3.2.4 Solutes

Three selected COCs were evaluated in the model simulations: tritium (^3H), iodine-129 (^{129}I), and carbon tetrachloride (CCl_4). The half-lives and solid-aqueous partition coefficients (K_d values) that were used for these COCs, and their maximum concentration limits (MCLs), are listed in Table 3.1.

Table 3.1. Half-lives and K_d values used for modeling selected contaminants of concern.

Contaminant of Concern	Half-life (yr)	K_d (cm^3/g)	MCL
Tritium	12.3	0	20,000 pCi/L
Carbon tetrachloride	680	0.011	0.005 mg/L
Iodine-129	1.57×10^7	0.3	1 pCi/L

Of the three COCs that were represented in the model simulations, tritium is the most mobile, with an assumed $K_d = 0 \text{ cm}^3/\text{g}$, but the least persistent owing to its relatively short half-life, $t_{1/2} = 12.3$ years. Carbon tetrachloride is the one of the primary targets for groundwater cleanup at the pump-and-treat (P&T) system in the 200 West Area. It is more strongly sorbed than tritium, with an assumed $K_d = 0.011 \text{ cm}^3/\text{g}$, and has a significantly longer half-life, $t_{1/2} = 680$ years. Iodine-129 is the least mobile, with an assumed $K_d = 0.3 \text{ cm}^3/\text{g}$, and has the longest half-life, $t_{1/2} = 1.57 \times 10^7$ years.

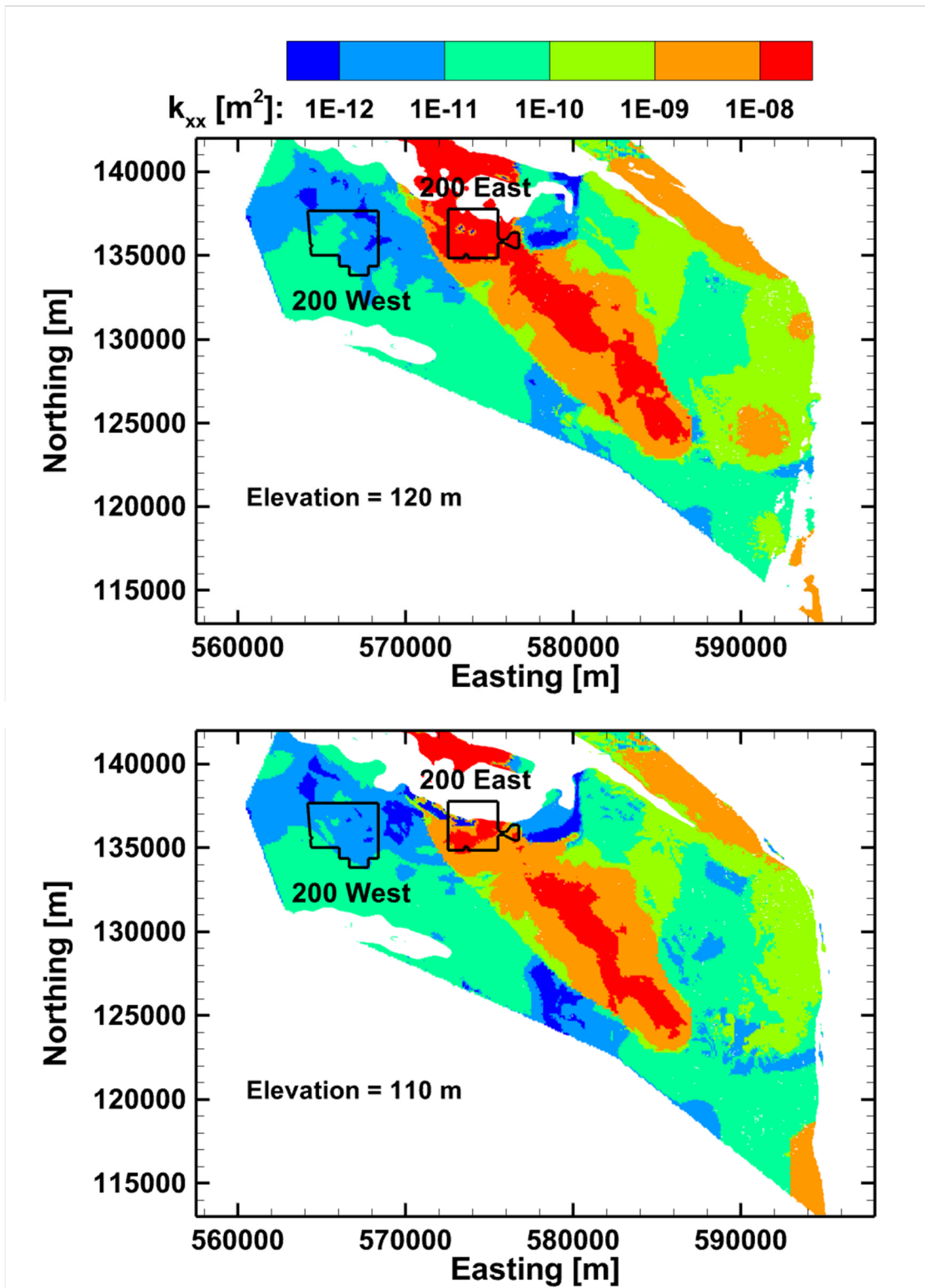


Figure 3.12. Permeability distributions at the 120 m (top) and 110 m (bot) elevations for the base model.

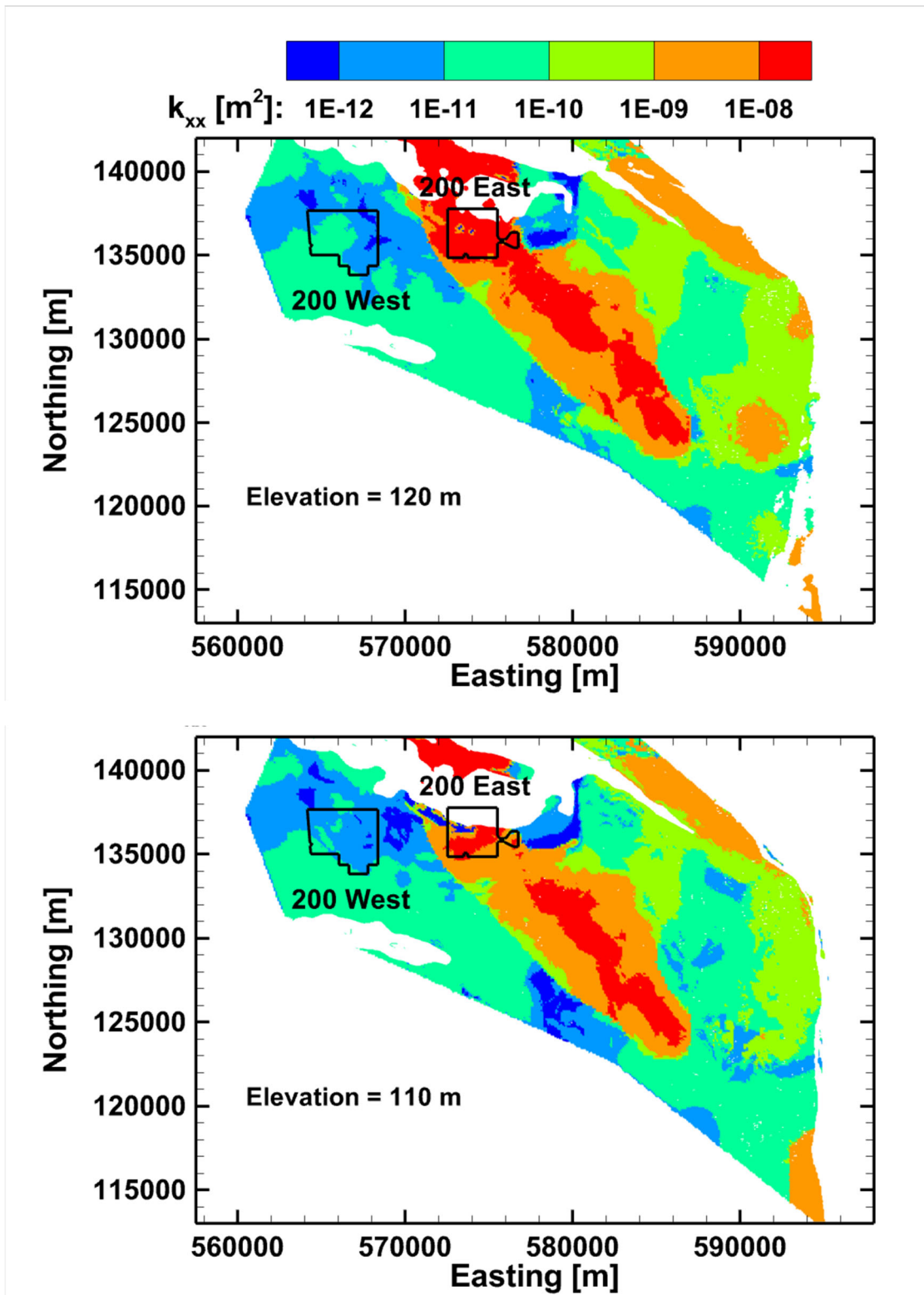


Figure 3.13. Permeability distributions at the 120-m and 110-m elevations for alternative model realization 0.

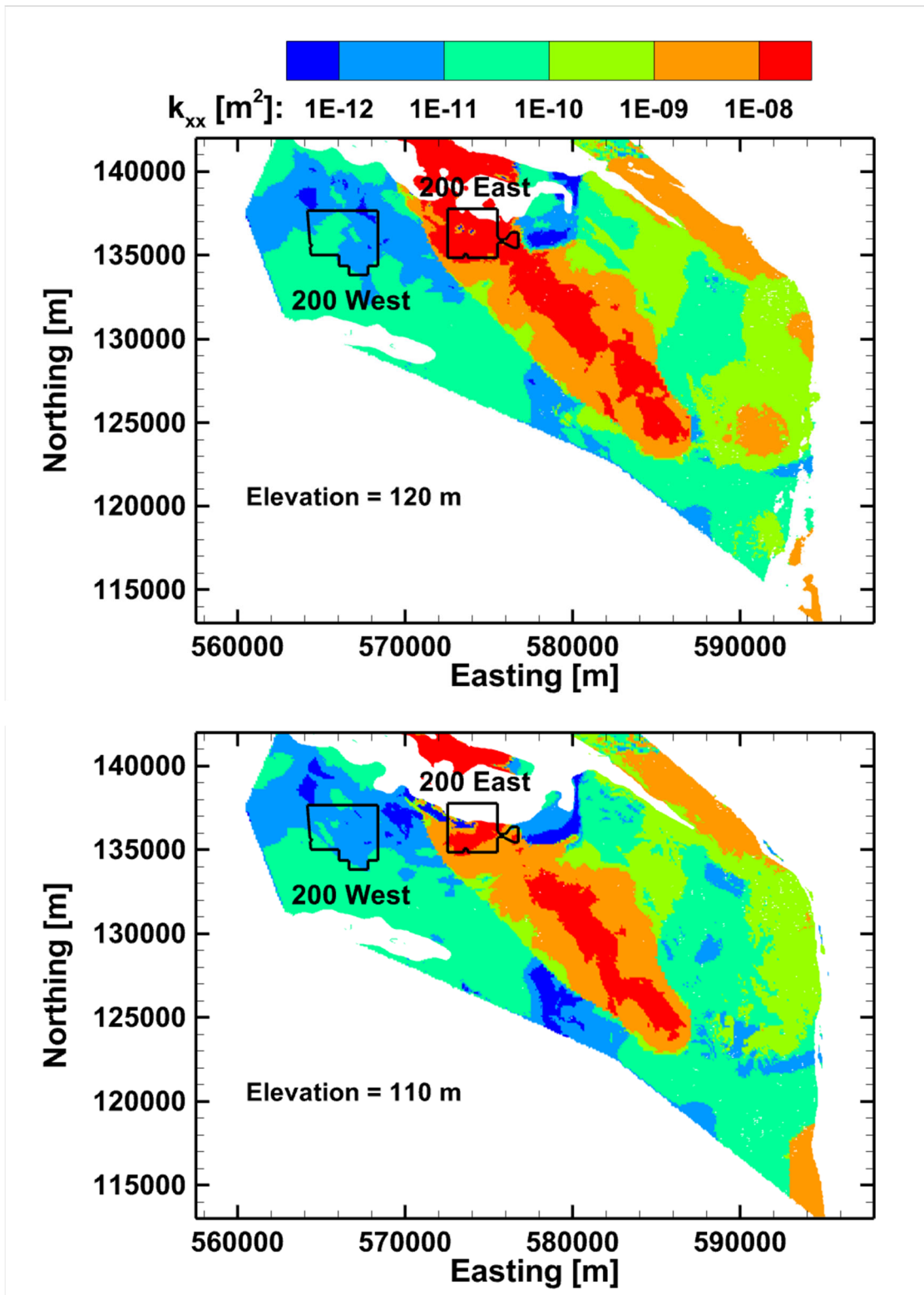


Figure 3.14. Permeability distributions at the 120-m and 110-m elevations for alternative model realization 4.

3.2.5 Initial and Boundary Conditions

Water level data from the Hanford Environmental Information System (HEIS) database were used to define initial aqueous pressures for the model simulations. Plume maps for the three selected COCs in 1993, originally generated by the Hanford site-wide groundwater monitoring program, were used to define initial solute concentration distributions. The concentrations from the plume maps were assigned to the first model layer below the water table in the eSTOMP models, and the same initial conditions were used in all of the models.

Constant Neuman-type (specified flux) boundary conditions were assigned to the upper and lower boundaries of the modeled domain. A uniform recharge rate of 3.5 mm/yr was used for the upper boundary. Actual recharge rates from net infiltration of meteoric water and other discharges of water at the ground surface are expected to vary across the site over space and time, according to surface soil type, vegetation conditions, disturbance, land use, and other site characteristics. (Fayer and Walters, 1995). However, model results were compared to a base case that used the same boundary conditions, and results were assessed in relative terms, so the use of a constant recharge rate was considered to be acceptable for the purposes of this study.

In addition to evaluating the potential influence of paleochannels, one of the original goals of this work was to evaluate the effects of uncertainties in recharge/discharge through basalt on model simulation results. Available data for piezometric head in basalt underlying the Hanford Site were reviewed and found to be very sparse relative to the area of the site. Reported estimates of the vertical hydraulic conductivity for basalt were also found to range over 10 orders of magnitude (Strait and Mercer, 1987; Spane and Vermeul, 1994). Due to this extreme variability and data sparsity, analysis of the effects of uncertainties in basalt recharge/discharge on flow and transport modeling results was not pursued further and no-flow conditions were assumed for the lower boundary in all of the models used in the current study. No-flow boundary conditions are also used for the top of basalt surface in the P2R model.

For the lateral boundaries in the eSTOMP models, dynamic “xyz-seepage face” boundary conditions were specified using linked-lists of boundary cell faces. This boundary condition uses a combination of Dirichlet (specified pressure) boundary conditions for cell faces in the linked lists that are below the water table, and Neuman (specified fluxes of zero, or no-flow conditions) for cell faces above the water table. Historical water level data from HEIS were used to define these dynamic boundary conditions. For solute transport, no-flow conditions were assumed for the upper and lower boundaries, and inflow-outflow conditions were specified for the lateral boundaries.

The base eSTOMP model and all of the alternative models were run using the recently-developed coupled well model capabilities in eSTOMP to simulate operations of 200 West P&T system over the period from 2012-2047. Operations of the 200 West P&T system began in 2012. The year 2047 is the end of the original 35-year operational period that was called for in the planned interim measure for groundwater cleanup by the 200 West P&T system (DOE, 2013). In the model simulations, well operations after year 2020 were assumed to be the same as in 2020. The modeled well network included the majority of wells in the 200 West P&T network, but excluded extraction wells located within the B-Complex of the 200 East Area. The well model had difficulty with convergence when those wells were included, owing to the thin aquifer in that portion of the domain.

Model “spin-up” simulations were performed first, without solute transport, for the period from time zero through 1993, to achieve quasi-steady-state flow conditions through the vadose zone portions of the model domains. Simulations with solute transport were then performed for the period from 1993-2500 using the 1993 groundwater COC plumes as initial conditions. No vadose sources of contaminants or artificial recharge were considered in the model simulations. Results are presented in the following section.

4.0 Results and Discussion

4.1 Tritium

Simulated groundwater tritium plumes at the 120-m elevation for the base case in 1993 and 2047 are displayed in Figure 4.1. The groundwater plume maps indicate that tritium had reached the Columbia River by or before 1993. Tritium has a relatively short half-life of 12.26 years, so by the year 2047 more than 4 half-lives would have passed. Simulation results show that most of the tritium plume that existed in 1993 has decayed to below the MCL by year 2047. A very small tritium plume with concentrations above the MCL is predicted to remain in 2047 between the 200 West and East areas.

Figure 4.2 (alternative model realization 0) and Figure 4.3 (alternative model realization 4) show tritium simulation results that are comparable to the results in Figure 4.1 (base model). The differences between the results obtained with the base case and with the alternative models are very subtle. This result is due, in part, to the modest increase in permeability that was used for the paleochannel features in the alternative models, but is also due to the short half-life of tritium, which results in relatively rapid shrinking of the plumes over time.

4.2 Carbon Tetrachloride

Figure 4.4, Figure 4.5, and Figure 4.6 show simulated carbon tetrachloride plumes for the base model and two alternative model realizations in years 1993 and 2200. The simulated plumes for the alternative model realizations exhibit slightly faster transport than the base model, as expected, due to their use of scaled-up permeability values. These models also depict what appears to be relatively narrow preferential flow paths that direct the movement of some of the carbon tetrachloride from the 200 West Area to the 200 East Area. Concentrations in portions of the plume are predicted to continue to exceed the MCL in 2200. However, in all cases, this simulated carbon tetrachloride groundwater plumes appear to remain largely within the area of the Central Plateau in 2200. The spatial moments of the simulated plumes were also computed (Section 4.4) to provide a quantitative means for comparing the results from the different models.

Figure 4.7 shows zoomed-in views of the simulated carbon tetrachloride plumes in the year 2200 for the base model and two alternative model realizations. The differences between the model results are more obvious in this figure, but still relatively small. Again, this is due primarily to the small increase in permeabilities that were applied to the paleochannel features relative to the base model.

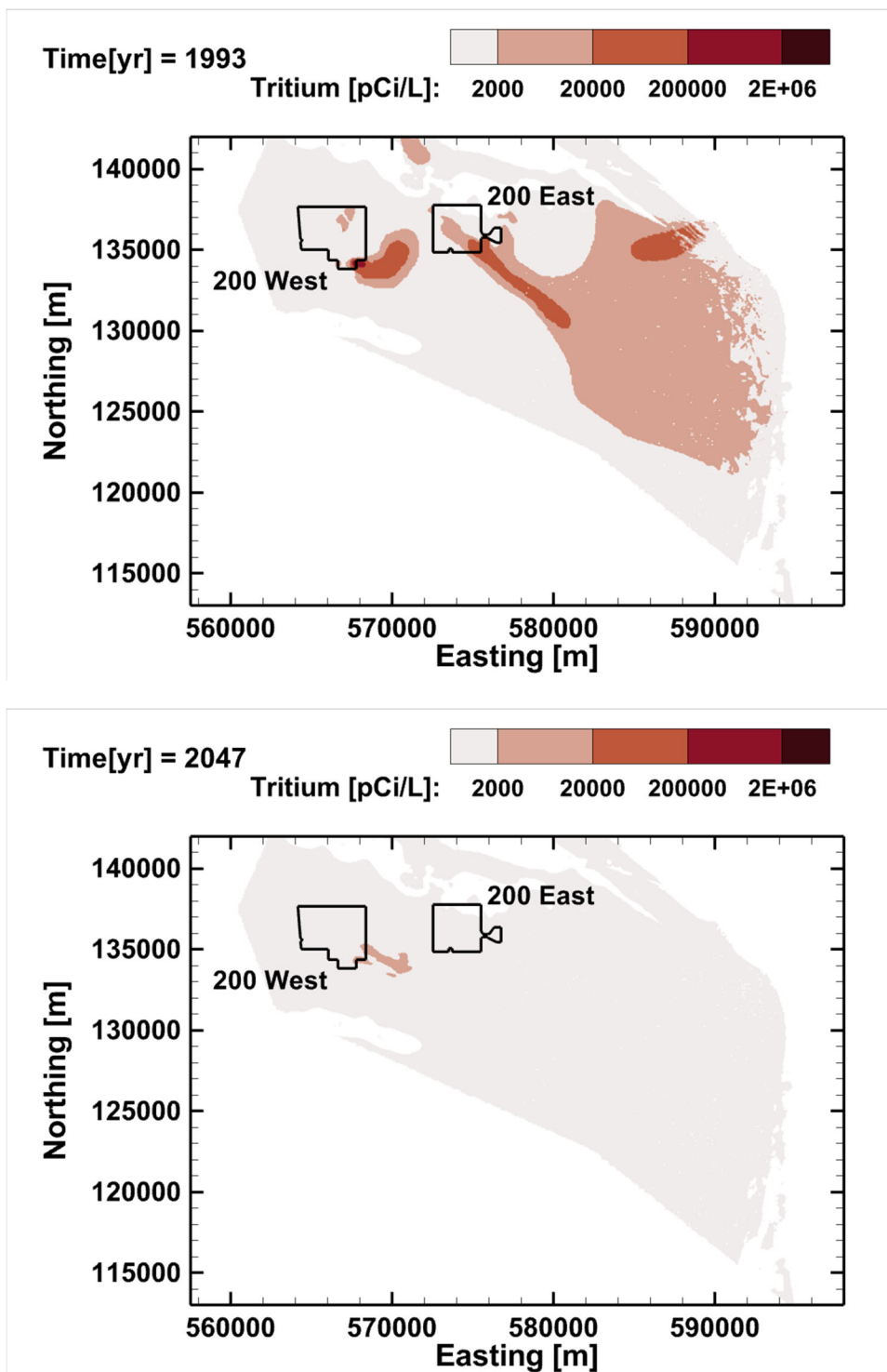


Figure 4.1. Simulated tritium distributions from the base case model at the 120-m elevation for years 1993 and 2047.

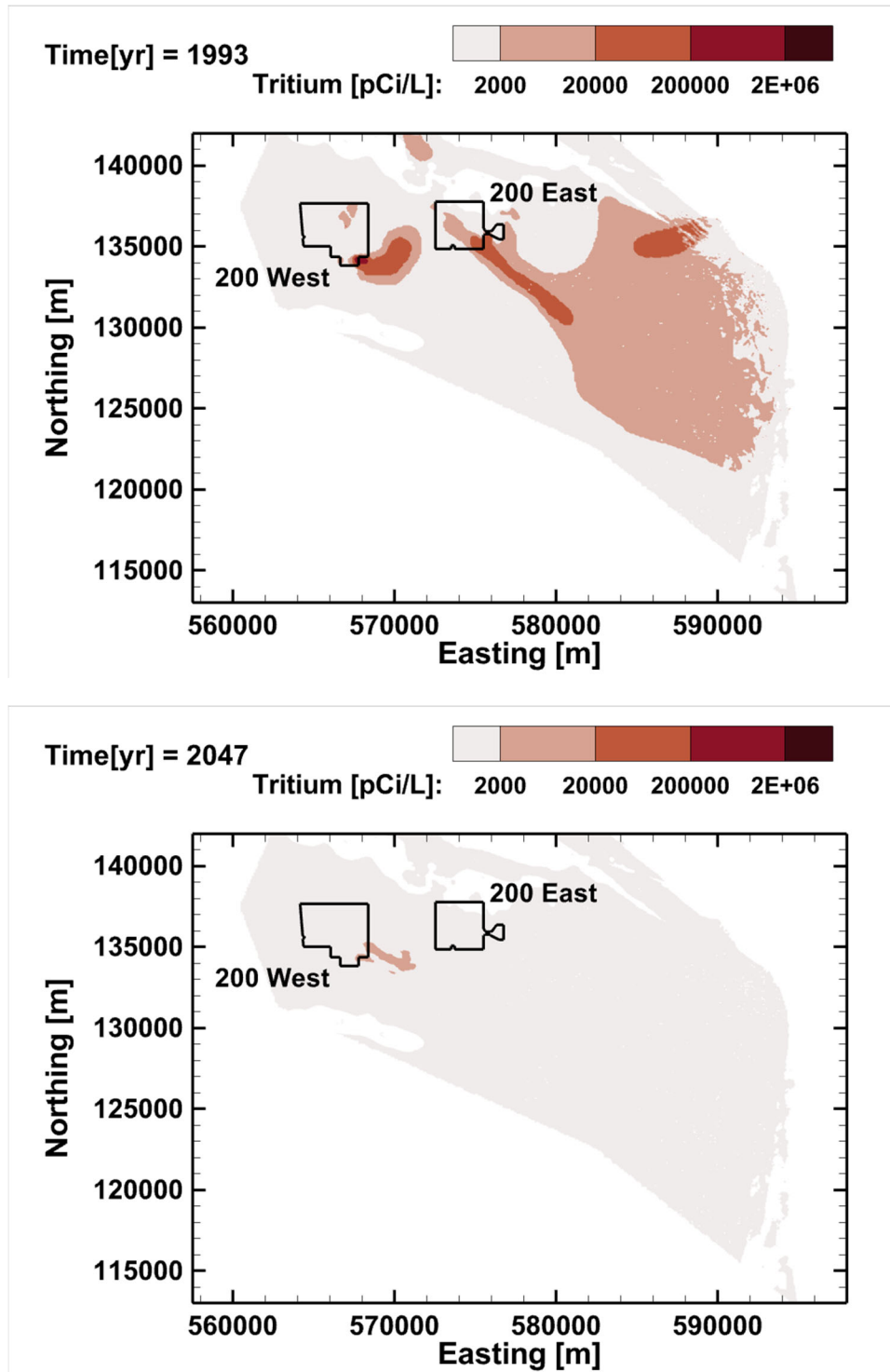


Figure 4.2. Simulated tritium distributions from alternative model realization 0 at the 120-m elevation for years 1993 and 2047.

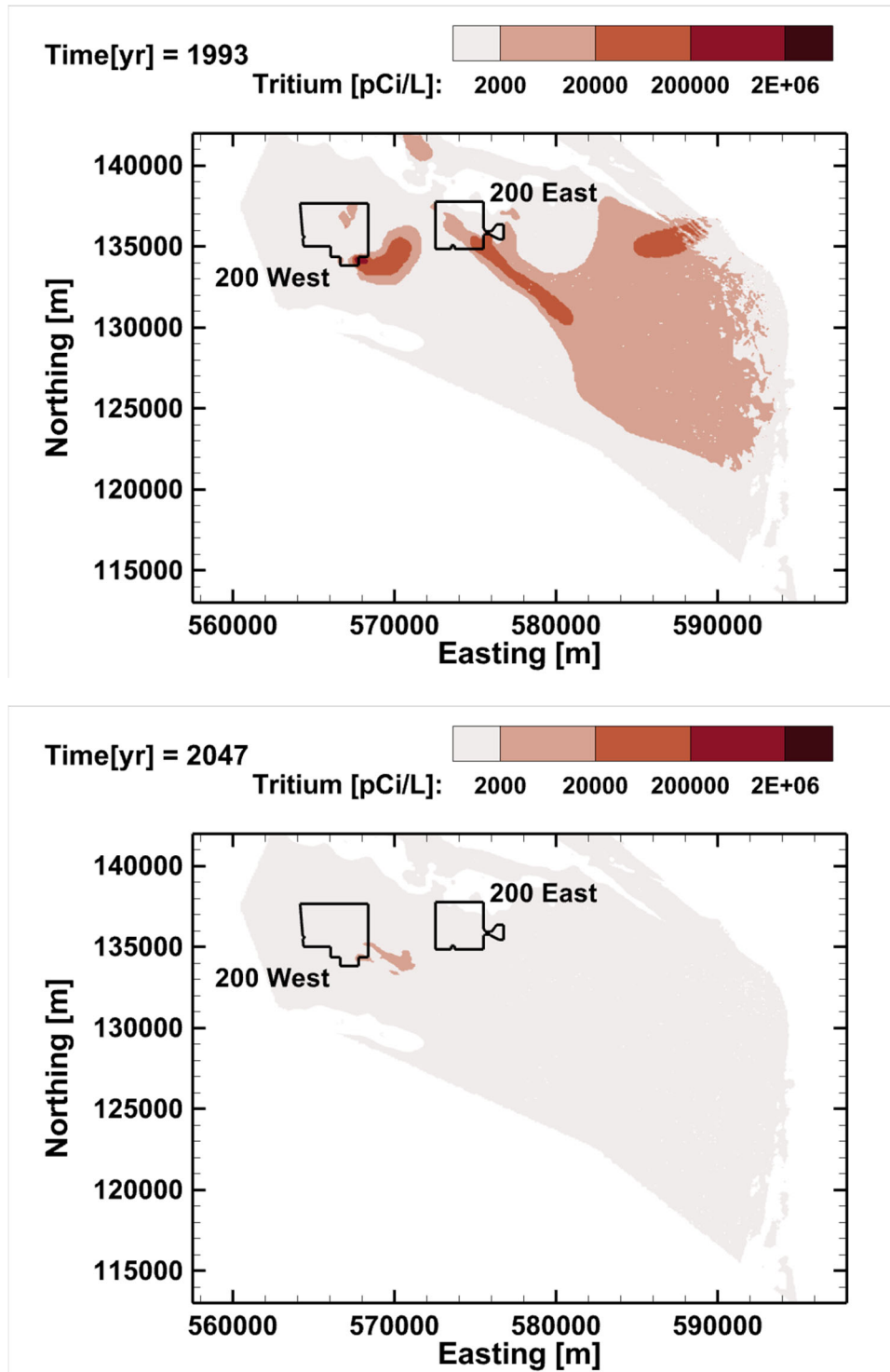


Figure 4.3. Simulated tritium distributions from alternative model realization 4 at the 120-m elevation for years 1993 and 2047.

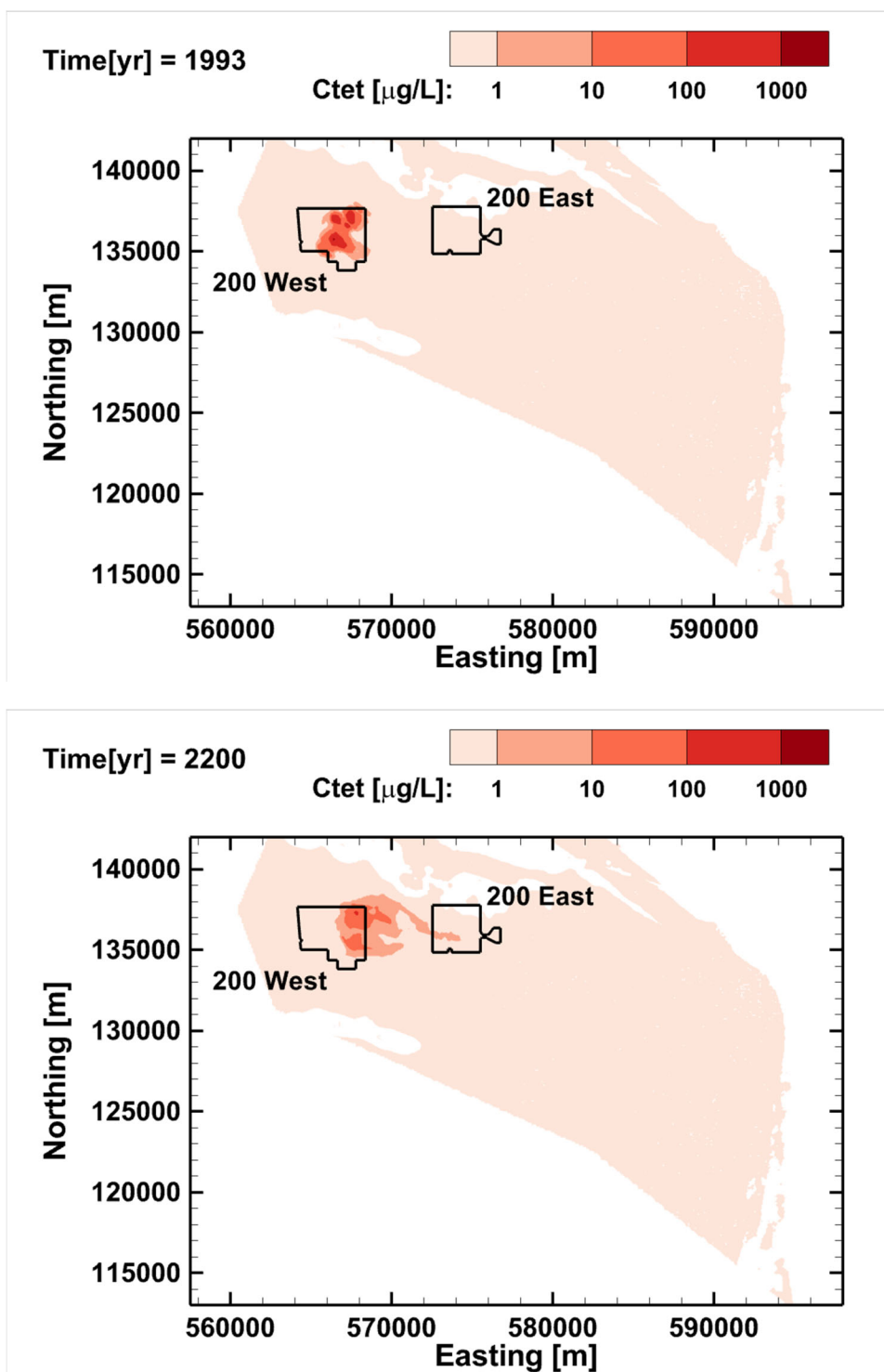


Figure 4.4. Simulated carbon tetrachloride concentrations from the base model at the 120-m elevation for years 1993 and 2200.

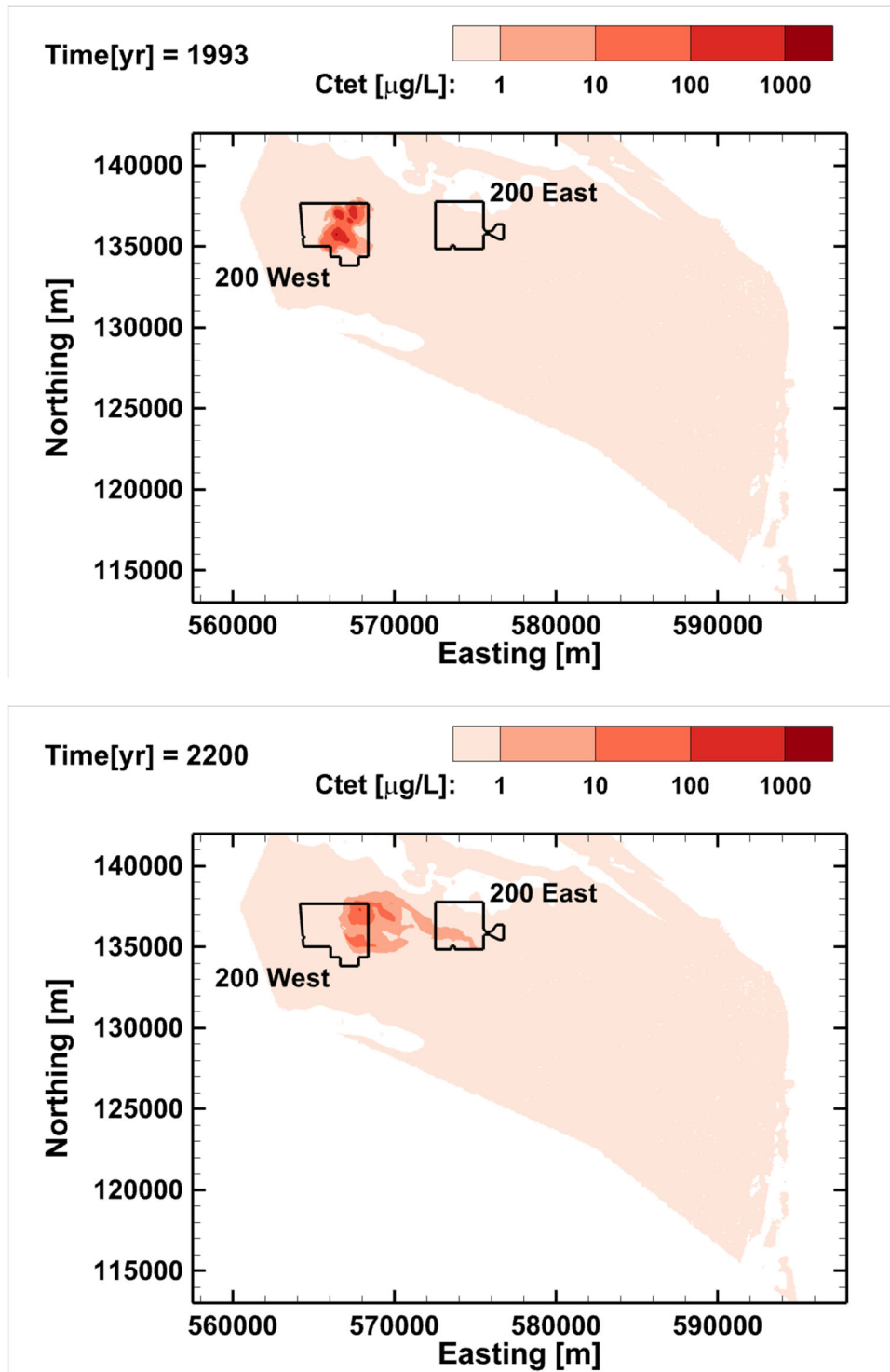


Figure 4.5. Simulated carbon tetrachloride concentrations from alternative model realization 0 at the 120-m elevation for years 1993 and 2200.

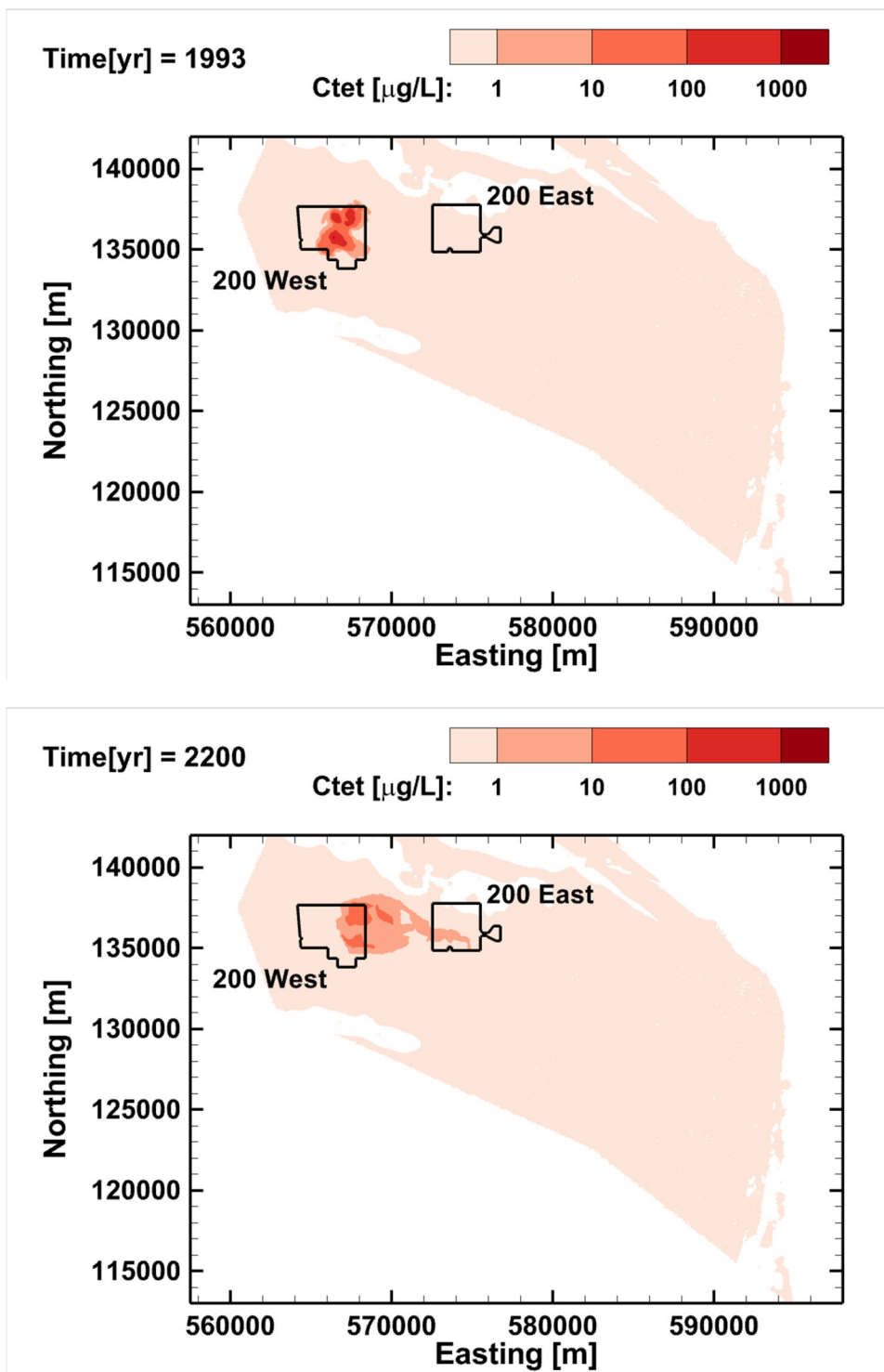


Figure 4.6. Simulated carbon tetrachloride concentrations from alternative model realization 4 at the 120-m elevation for years 1993 and 2200.

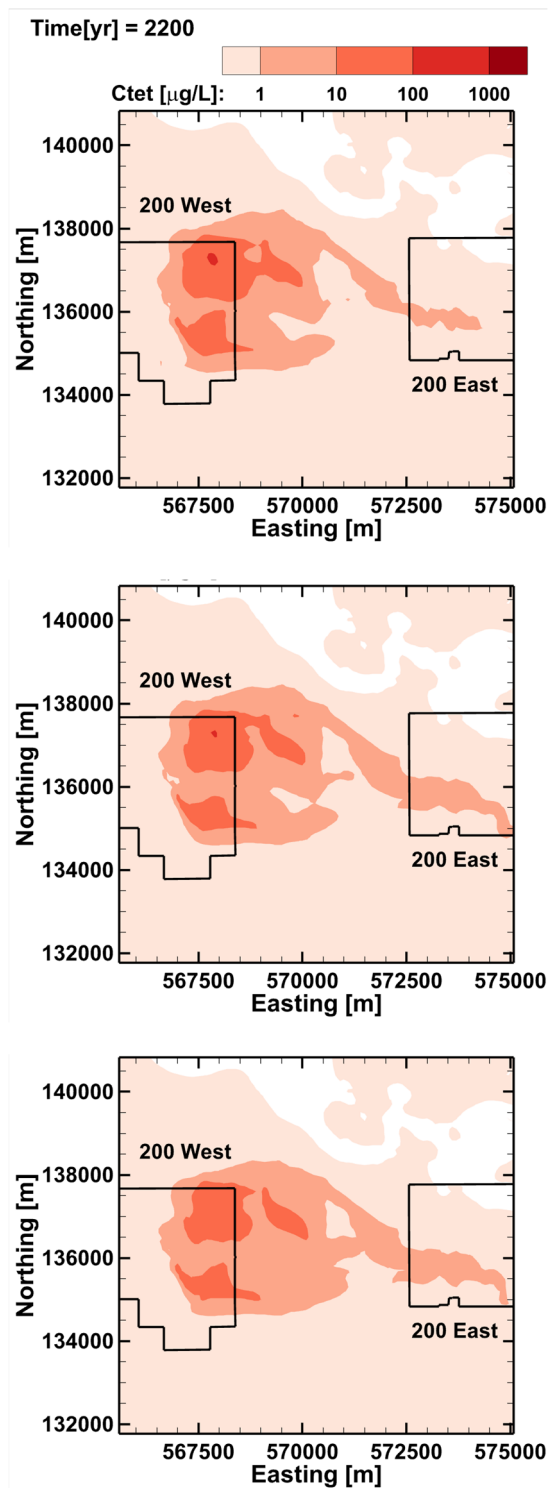


Figure 4.7. Zoomed-in views of simulated carbon tetrachloride plumes in the year 2200 for the base model (top), alternative model realization 0 (middle), and alternative model realization 4 (bottom).

4.3 Iodine-129

Multiple iodine-129 plumes exist on the Hanford Site (Figure 4.8). The one with the largest spatial extent originated in the 200 East Area and extends diagonally across the 200 East Area and to the east and southeast towards the Columbia River. This plume, labeled the *i129_3* plume in Figure 4.8, is relatively dilute. The second largest iodine-129 plume, and the one with the highest concentrations, is labeled *i129_2* plume in Figure 4.8. This plume is located near the southeast corner of the 200 West Area, in the 200-UP-1 operable unit. A third and much smaller iodine-129 plume, labeled *i129_1* in Figure 4.8, is located in the 200 West Area, within the 200-ZP-1 operable unit.

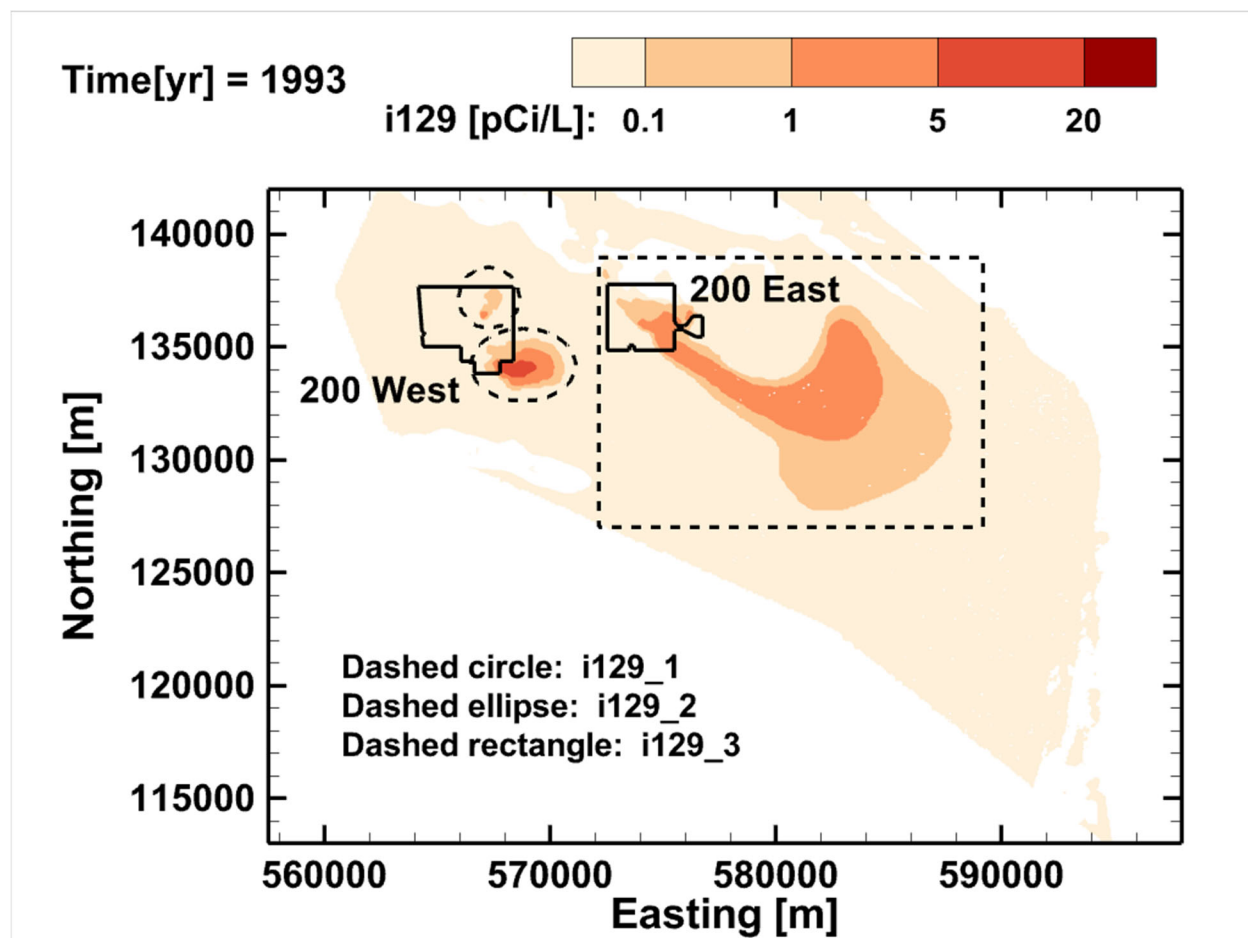


Figure 4.8. Locations of three separate iodine-129 plumes on the Hanford Site in 1993.

Figure 4.9, Figure 4.10, and Figure 4.11 show iodine-129 simulation results for the base model and for alternative model realizations 0 and 4 for years 1993 and 2200. The results for all the models are very similar, and show that by the year 2200 the *i129_3* plume is predicted to have become more dispersed and to have migrated to the Columbia River. Predicted concentrations for the *i129_2* plume in year 2200 appear to be mostly below the 1pCi/L MCL. By year 2200, the *i129_2* plume is predicted to have migrated across the southern part of the 200 East Area, but still be largely contained within the area of the Central Plateau. Predicted plume concentrations for the *i129_2* plume in year 2200 are mostly less than 5 pCi/L. Relatively little change is predicted for the *i129_1* plume located in the 200-ZP-1 operable unit.

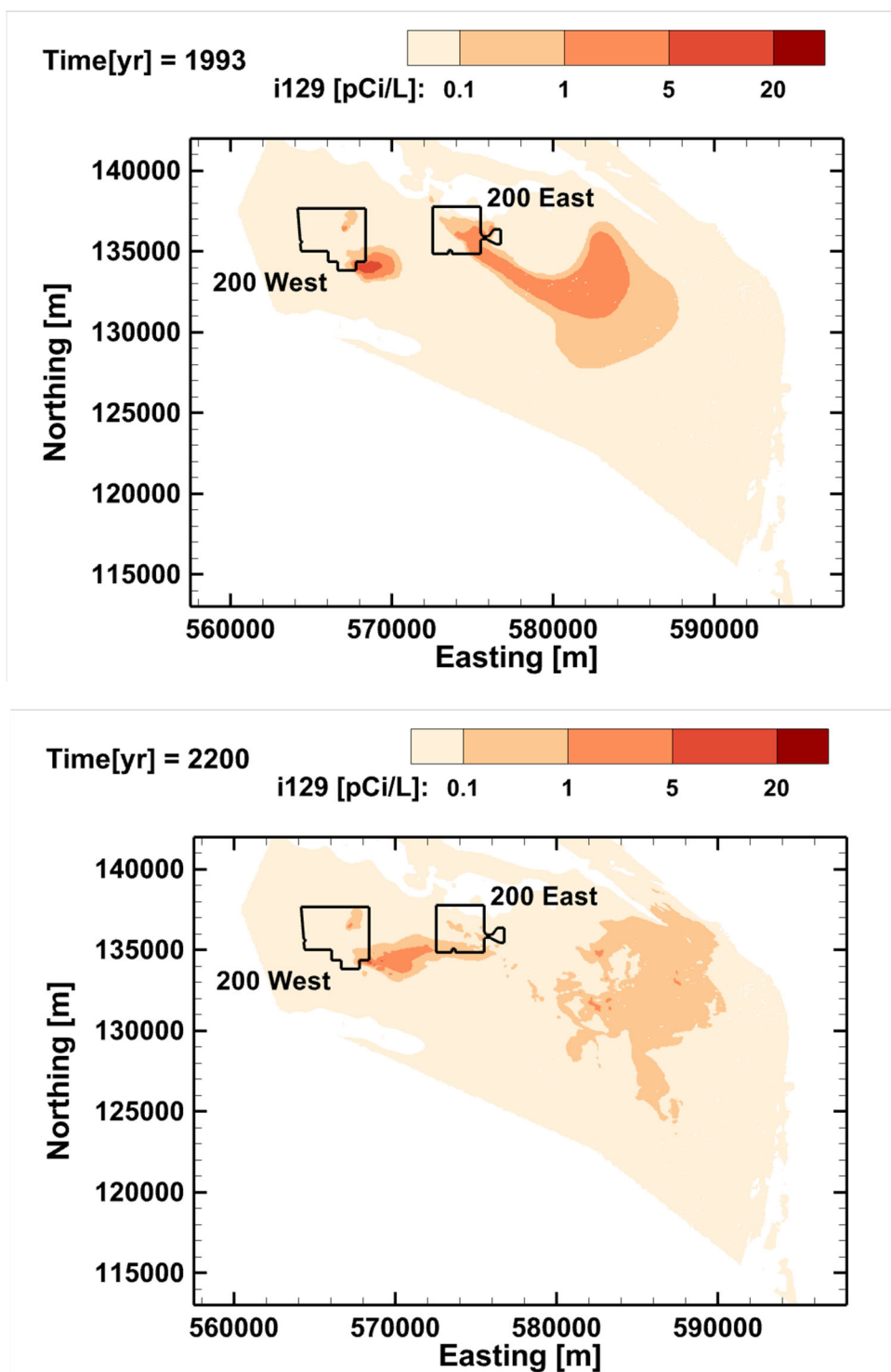


Figure 4.9. Simulated iodine-129 concentrations for the base model at the 120-m elevation for years 1993 and 2200.

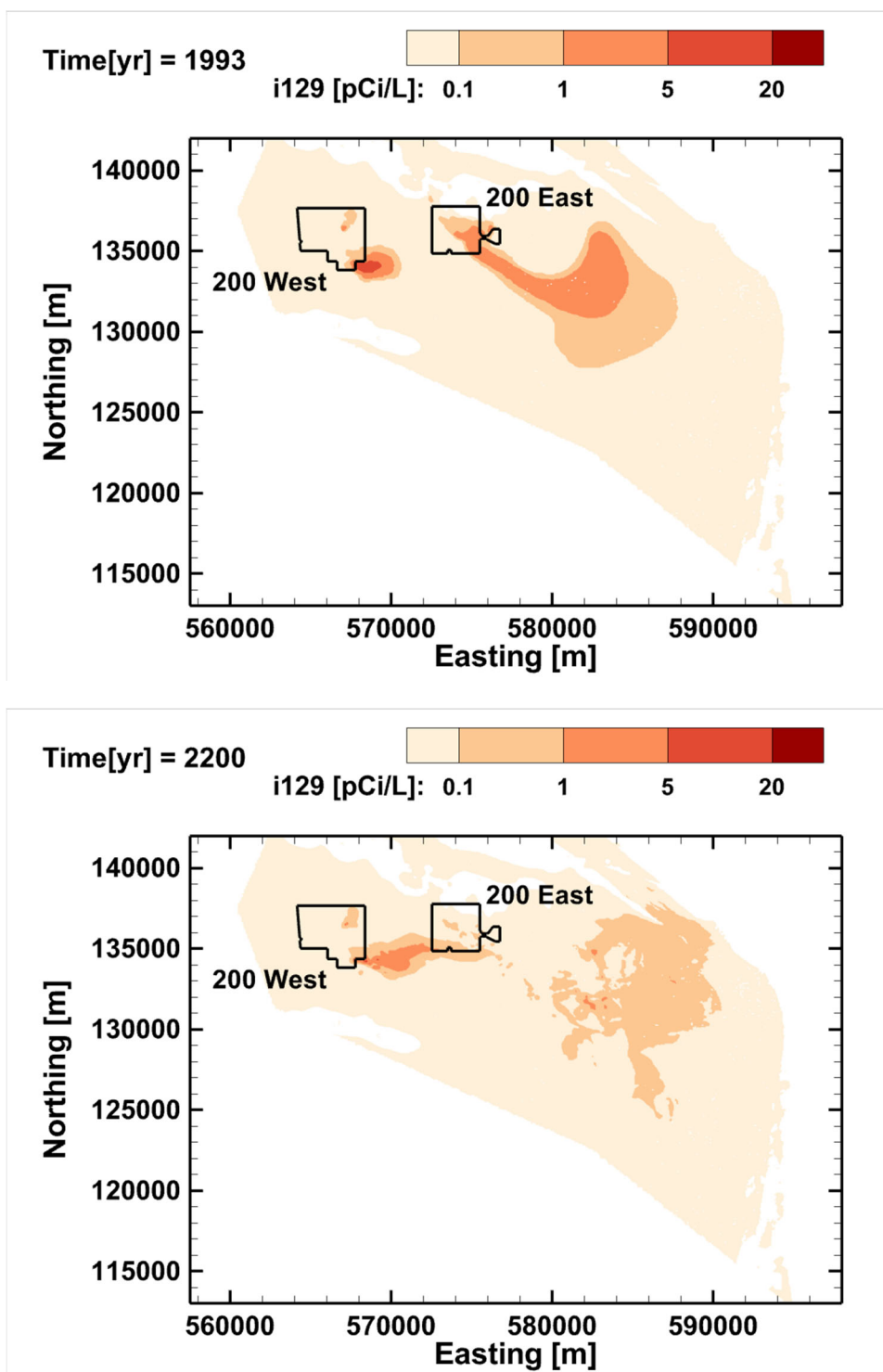


Figure 4.10. Simulated iodine-129 concentrations for alternative model realization 0 at the 120-m elevation for years 1993 and 2200.

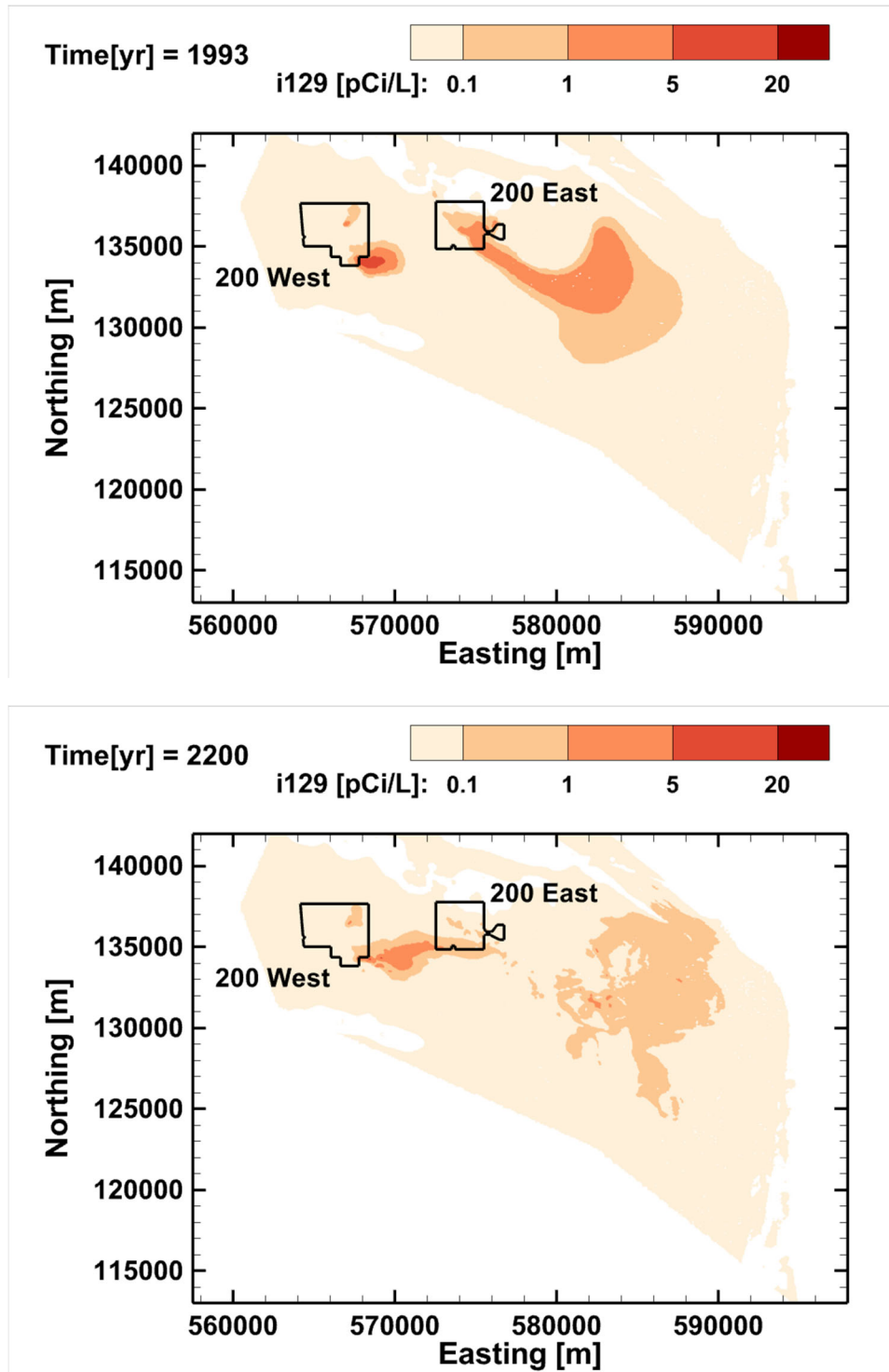


Figure 4.11. Simulated iodine-129 concentrations for alternative model realization 4 at the 120-m elevation for years 1993 and 2200.

Figure 4.12 shows zoomed-in views of the simulated iodine-129 plumes in the year 2200 for the base model and two alternative model realizations. Differences between model results are again more obvious in this figure, but still relatively small. Differences between base and alternative model results appear relatively smaller than for carbon tetrachloride because of differences in K_d values and local flow fields.

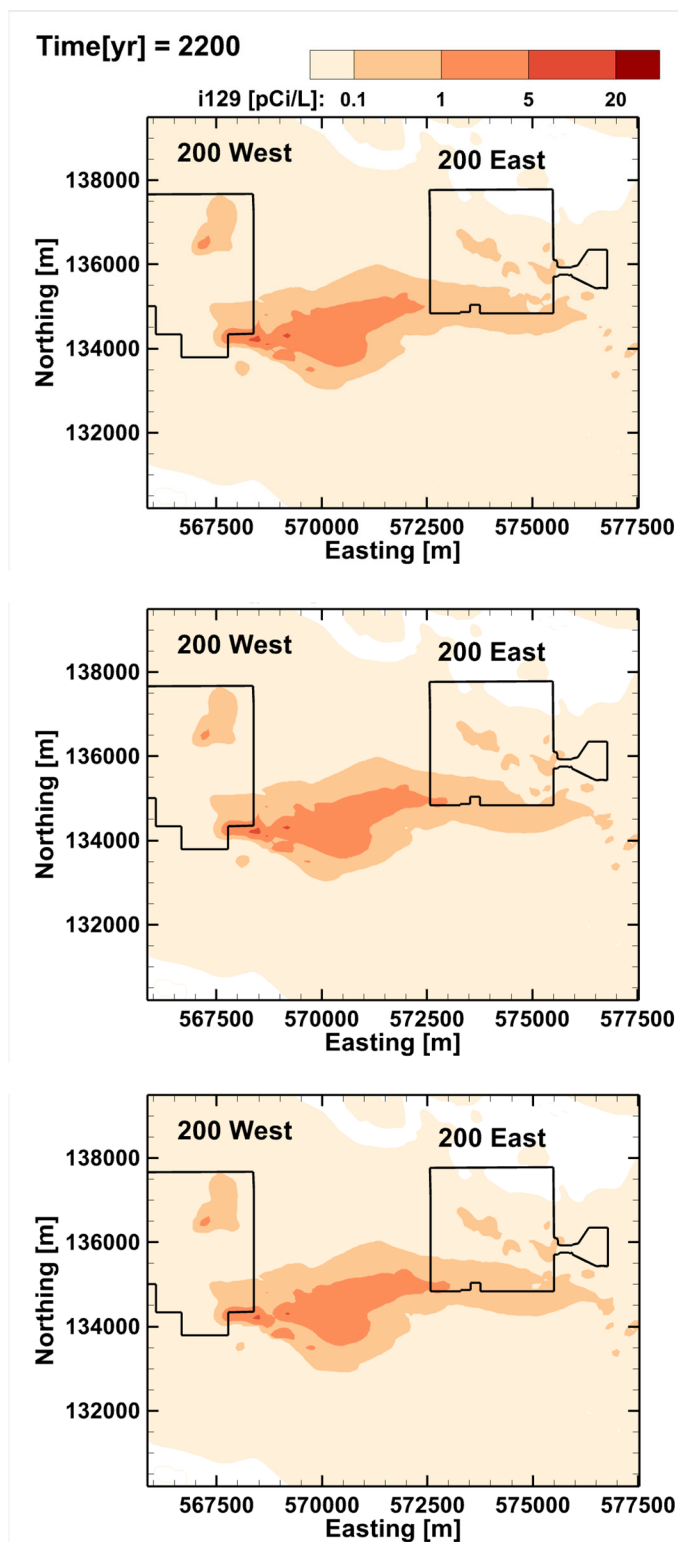


Figure 4.12. Zoomed-in views of simulated iodine-129 plumes in the year 2200 for the base model (top), alternative model realization 0 (middle), and alternative model realization 4 (bottom).

4.4 Spatial Moment Analysis

The simulated plumes for the base case and the alternative model realizations are qualitatively very similar. The normalized spatial moments of the simulated solute plumes were also calculated to compute plume trajectories and velocities, and to provide a quantitative basis for comparing results from the different simulation cases.

The ijk^{th} moment of the solute concentration distribution in space was defined as

$$M_{ijk}(t) = \int_{-\infty}^{\infty} \int_{-\infty}^{\infty} \int_{-\infty}^{\infty} \theta C(x, y, z, t) x^i y^j z^k dx dy dz \quad (4.1)$$

where θ is the volumetric water content, C is the solute concentration in the aqueous phase, and x , y , and z are the spatial coordinates (Freyberg, 1986). The integrals in Eq. (4.1) were evaluated over the extent of the 3D model domain, excluding inactive regions.

The zeroth, first, and second ($i + j + k = 0, 1$, or 2 , respectively) spatial moments of the solute plumes were computed. These moments provide measures of the total mass, center of mass, and spread of the solute plume about its center of mass. The zeroth moment, M_{000} , is equal to the total mass in the domain. The first moment, normalized by the zeroth moment, defines the location of the center of mass (x_c, y_c, z_c):

$$x_c = \frac{M_{100}}{M_{000}} \quad y_c = \frac{M_{010}}{M_{000}} \quad z_c = \frac{M_{001}}{M_{000}} \quad (4.2)$$

The second moment about the center of mass defines a spatial covariance tensor:

$$\sigma^2 = \begin{bmatrix} \sigma_{xx}^2 & \sigma_{xy}^2 & \sigma_{xz}^2 \\ \sigma_{yx}^2 & \sigma_{yy}^2 & \sigma_{yz}^2 \\ \sigma_{zx}^2 & \sigma_{zy}^2 & \sigma_{zz}^2 \end{bmatrix} \quad (4.3)$$

$$\sigma_{xx}^2 = \frac{M_{200}}{M_{000}} - x_c^2 \quad \sigma_{yy}^2 = \frac{M_{020}}{M_{000}} - y_c^2 \quad \sigma_{zz}^2 = \frac{M_{002}}{M_{000}} - z_c^2$$

$$\sigma_{xy}^2 = \sigma_{yx}^2 = \frac{M_{110}}{M_{000}} - x_c y_c \quad \sigma_{xz}^2 = \sigma_{zx}^2 = \frac{M_{101}}{M_{000}} - x_c z_c \quad \sigma_{yz}^2 = \sigma_{zy}^2 = \frac{M_{011}}{M_{000}} - y_c z_c$$

The components of the covariance tensor are directly related to the spread of the solute plume about its center of mass and can be related to the components of an effective dispersion tensor (Freyberg, 1986).

Figure 4.13 shows the evolution of the location of the centers of mass (x_c, y_c) for the carbon tetrachloride and the *i129_2* plumes, between years 1993 and 2500. As shown by the previous plume plots, the simulated tritium plumes have largely disappeared by the year 2047 owing to the short half-life of tritium. Therefore, the spatial moment results for tritium were not computed. For the other two COCs that were evaluated here, each colored symbol in Figure 4.13 represents a different simulation case, and each group of symbols represents the variability in the locations of the center of mass of the plumes at different times.

The last four clusters shown in these plots represent, from right to left, years 2500, 2400, 2300, and 2200. Figure 4.13 shows that the trajectories of the plumes are similar for all simulation cases, but there is some variability in the distances traveled. At year 2500, the calculated average and standard deviation of the distances between the predicted centers of mass for the base case versus the five alternative model realizations for the carbon tetrachloride plumes are 1088 m and 520 m, respectively. At year 2500, the calculated average and standard deviation of the distances between the predicted centers of mass for the base case versus the five alternative realizations for the *i129_2* plumes are 386 m and 319 m, respectively. Variability in simulated plume trajectories and travel distances is expected to increase with more realizations of alternative models with paleochannel features, and with more variability in the permeabilities of the paleochannel features relative to the base case.

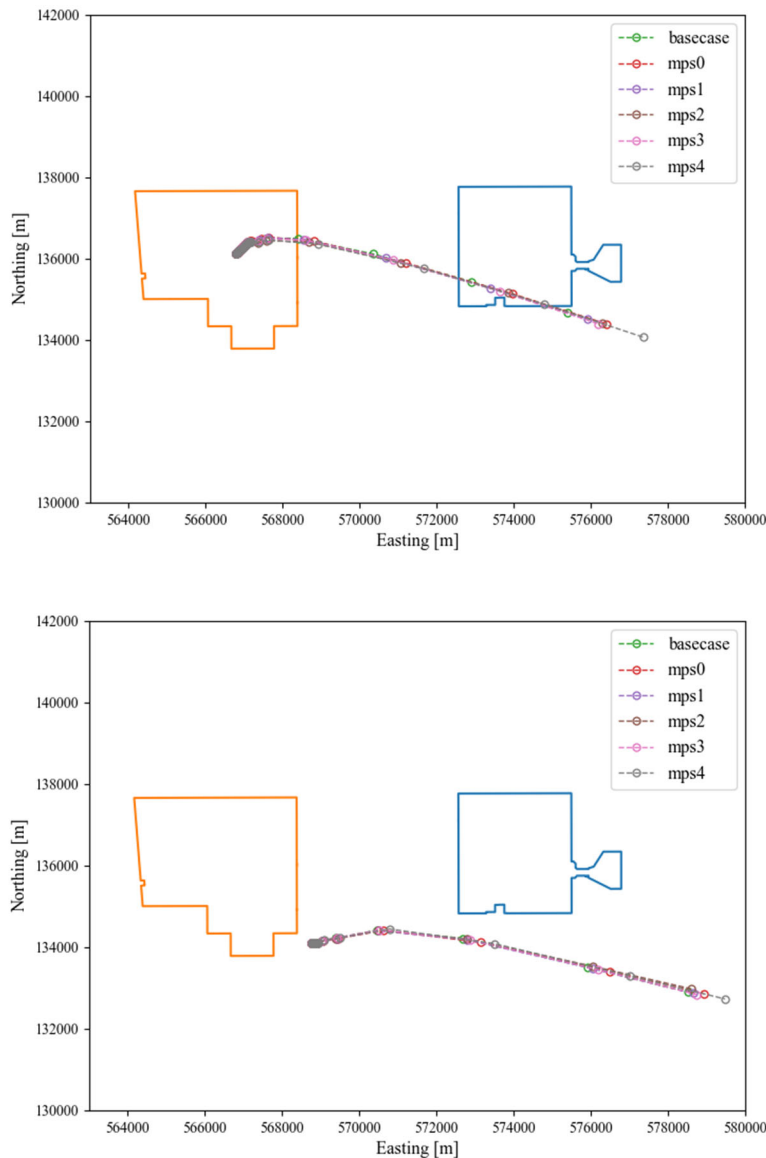


Figure 4.13. Calculated locations of the centers of mass (x_c , y_c) for the simulated carbon tetrachloride (top) and iodine-129 (bottom) plumes between year 1993 and 2500. In the figure legend, *basecase* refers to the base reference case model results and *mps0*, *mps1*, *mps2*, *mps3*, and *mps4* refer to results from alternative model realizations.

5.0 Summary and Conclusions

A methodology was developed and demonstrated for generating alternative conceptual-mathematical models of the Hanford subsurface for modeling groundwater flow and contaminant transport. The methodology uses an MPS framework and a TI developed from LiDAR-based digital elevation (topography) data for the Hanford Site. The LiDAR data show outlines of relic paleochannel features that were formed by the ancestral Columbia River and flooding events in the past. These relic paleochannel features are assumed to be representative of similar paleochannel features that exist in the subsurface and influence water flow and contaminant transport behavior. Binned grain-size distribution metrics from selected borehole samples, and ERT data from selected measurement transects, were also used, as hard and soft data, respectively, by the MPS algorithm. The methodology reproduces the general shapes of the relic paleochannel features visible in the LiDAR-based topography data and honors the hard data at their specified locations. Multiple realizations of paleochannel features were generated and superimposed on a base or reference model to produce alternative conceptual-mathematical models of the subsurface.

Numerical simulations of water flow and transport of selected COCs were performed with eSTOMP using a reference model, based on the MODFLOW- and MT3D-based P2R model of the Hanford Site (Budge, 2020), and with multiple realizations of alternative models that contain paleochannel features generated by MPS. Simulations were performed with each model for COCs – tritium, carbon tetrachloride, and iodine-129 – over the time period from 1993 to 2500.

To provide a simple illustration of the potential effects of paleochannels on transport results, the permeabilities assigned to the paleochannel features were scaled up by a factor of 1.5 relative to the permeabilities used in the base reference model. The resulting variability in model simulation results was relatively small, but the results still demonstrate how paleochannel features might affect flow and transport behavior. Greater variability in simulation results would likely occur if more realizations of the alternative models with paleochannel features were used, and if the permeability contrast of the paleochannel features over the background materials was larger.

The simulated plumes from all of the models were similar for a given COC, but the alternative models containing paleochannel features exhibited faster transport. The trajectories of the centers of mass of the simulated carbon tetrachloride plumes followed nearly the same path, but travel distances varied between the simulation cases. At year 2500, the calculated average and standard deviation of the distances between the predicted centers of mass for the base case versus the five alternative model realizations for the carbon tetrachloride plumes are 1088 m and 520 m, respectively. Similarly, the trajectories of the centers of mass for the simulated iodine-129 plumes also followed nearly the same paths, but travel distances again varied by simulation case. At year 2500, the calculated average and standard deviation of the distances between the predicted centers of mass for the base case versus the five alternative realizations for the *i129_2* plumes are 386 m and 319 m, respectively. The paths followed by the simulated carbon tetrachloride and iodine-129 plumes were different, owing to different starting locations for the plumes and variability of the flow field in different parts of the model domain.

The ERT and grain-size distribution data that were used in this study were selected because of the availability of ERT data for certain areas, and the availability of grain-size distribution data for locations in proximity to those areas. Grain-size distribution data from additional wells located in the 200 East Area were also used because the wells are located within an area identified as part of the HCZ in the P2R model (Budge, 2020). During FY22, additional ERT, as well as seismic velocity data, were generated in several areas on both the Central Plateau and to the southeast of the Plateau. These new geophysical data sets, and any other grain-size distribution data that might be available for boreholes and wells near those

survey line locations, and elsewhere, could potentially be used in future applications of the described methodology.

Some limitations of this study include the following:

1. To develop the TI, it was assumed that the relic paleochannel features that are visible in the LiDAR data are representative of similar features in the subsurface elsewhere. However, the relic paleochannel features visible in the LiDAR data date to the late Pleistocene or early Holocene and represent lower-energy flow regimes relative to earlier flood events. Therefore, the size and orientations of the paleochannel features in the subsurface that were formed by earlier flood events may differ from those that are evident in the LiDAR data. Larger channels oriented more in line with the flow direction would result in faster transport toward the river.
2. A single threshold was used to segment grain size distribution metrics for samples collected from selected boreholes and wells to define paleochannel and non-paleochannel classes that were used as hard (known) data. In reality, channel-fill materials can be composed of a range of grain sizes. Our basic assumption was that paleochannel sediments would generally be coarser than non-paleochannel sediments. A single threshold was used for demonstration, but multiple thresholds could also be used to represent multiple classes of sediments.
3. Like the grain-size distribution metrics, a single threshold was used to segment bulk EC data from ERT results to define paleochannel and non-paleochannel sediments. The thresholds chosen for both the grain-size distribution metrics and the ERT data were based on a very limited set of laboratory experimental data relating bulk EC and grain-size distribution metrics for repacked mixtures of Hanford sediments. Additional petrophysical data are needed to corroborate and/or refine these relationships. In general, an effort focused on generating petrophysical data is needed to better use recently acquired geophysical data sets collected at Hanford.

6.0 Quality Assurance

This work was performed in accordance with the Pacific Northwest National Laboratory Nuclear Quality Assurance Program (NQAP). The NQAP complies with the DOE Order 414.1D, "Quality Assurance." The NQAP uses NQA-1-2012, "Quality Assurance Requirements for Nuclear Facility Application," as its consensus standard and NQA-1-2012 Subpart 4.2.1 as the basis for its graded approach to quality.

7.0 References

- BHI-01573. 2001. The Groundwater/Vadose Zone Integration Project: The Application of Features, Events, and Process Methodology at the Hanford Site. Rev. 0, Bechtel Hanford Inc., Richland, Washington.
- Bjornstad, B. N. 2006. On the Trail of the Ice Age Floods – A Geological Field Guide to the Mid-Columbia Basin. Keokee Books, Sandpoint, Idaho.
- Budge, T. J. 2020. Model Package Report: Plateau to River Groundwater Model, Version 8.3. CP-57037, Rev. 2, CH2MHill Plateau Remediation Company, Richland, Washington.
- Deutsch, C. V., and T. T. Tran. 2002. “Fluvsim: A Program for Object-Based Stochastic Modeling of Fluvial Depositional Systems.” *Computers & Geosciences* 28 (4): 525-535. [https://doi.org/10.1016/s0098-3004\(01\)00075-9](https://doi.org/10.1016/s0098-3004(01)00075-9).
- DOE. 2013. Hanford Site Cleanup Completion Framework. DOE/RL-2009-10, Rev. 1, U.S. Department of Energy, Richland Operations Office, Richland, Washington.
- DOE Order 414.1D, “Quality Assurance.” U.S. Department of Energy, Washington, D.C.
- Fang, Y., D. Appriou, D. H. Bacon, V. Freedman, M. L. Rockhold, C. Ruprecht, G. Tartakovsky, M. D. White, S. K. White, and F. Zhang. 2018. eSTOMP Online User Guide. Accessed on September 9, 2021 at http://stomp.pnnl.gov/estomp_guide/eSTOMP_guide.stm (last update March 2015).
- Fayer, M. J., and T. B. Walters. 1995. Estimated Recharge Rates at the Hanford Site. PNL-10285, Pacific Northwest Laboratory, Richland, Washington.
- Fecht, K. R., T. E. Marceau, B. N. Bjornstad, D. G. Horton, G. V. Last, R. E. Peterson, S. P. Reidel, and M. M. Valenta. 2004. Late Pleistocene- and Holocene-Age Columbia River Sediments and Bedforms: Hanford Reach Area, Washington. Part 1 Geologic Atlas Series. BHI-01648, Rev .0, Bechtel Hanford, Inc., Richland, Washington.
- Fecht, K. R., and T. E. Marceau. 2006. Late Pleistocene- and Holocene-Age Columbia River Sediments and Bedforms: Hanford Reach Area, Washington. Part 2 Geologic Atlas Series. WCH-46, Rev. 0, Washington Closure Hanford, Richland, Washington.
- Freyberg, D. L. 1986. “A Natural Gradient Experiment on Solute Transport in a Sand Aquifer: 2. Spatial Moments and the Advection and Dispersion of Nonreactive Tracers.” *Water Resources Research* 22 (13): 2031-2046. <https://doi.org/10.1029/WR022i013p02031>
- Hansen, T. M., L. T. Vu, T. Bach. 2016. “MPSLIB: A C++ Class for Sequential Simulation of Multiple-Point Statistical Models.” *SoftwareX* 5: 127-133. <https://doi.org/10.1016/j.softx.2016.07.001>
- Hansen, T. M., L. T. Vu, K. Mosegaard, and K. S. Cordua. 2018. “Multiple Point Statistical Simulation Using Uncertain (Soft) Conditional Data.” *Computers & Geosciences* 114: 1-10. <https://doi.org/10.1016/j.cageo.2018.01.017>
- Hammond, T. B. 2015. Development of the Hanford South Geologic Framework Model, Hanford Site, Washington. ECF-Hanford-13-0029, Rev. 1, CH2M Hill, Richland, Washington.

- Last, G. V., V. J. Rohay, F. J. Schelling, A. L. Bunn, M. A. Delamare, R. L. Dirkes, R. D. Hildebr, J. G. Morse, B. A. Napier, R. G. Riley, L. Soler, and P. D. Thorne. 2004. "A Comprehensive and Systematic Approach to Developing and Documenting Conceptual Models of Contaminant Release and Migration at the Hanford Site." *Stochastic Environmental Research and Risk Assessment (SERRA)* 18 (2): 109-116. <https://doi.org/10.1007/s00477-003-0144-6>
- Madsen, R. B., H. Kim, A. J. Kallesøe, P. B. E. Sandersen, T. N. Vilhelmsen, T. M. Hansen, A. V. Christiansen, I. Møller, and B. Hansen. 2021. "3D Multiple-Point Geostatistical Simulation of Joint Subsurface Redox and Geological Architectures." *Hydrology and Earth System Sciences* 25 (5): 2759-2787. <https://doi.org/10.5194/hess-25-2759-2021>
- Mariethoz, G., P. Renard, and J. Straubhaar. 2010. "The Direct Sampling Method to Perform Multiple-Point Geostatistical Simulations." *Water Resources Research* 46 (11). <https://doi.org/10.1029/2008wr007621>
- Miall, A. 2014. "The Facies and Architecture of Fluvial Systems." In *Fluvial Depositional Systems*, 9-68. https://doi.org/10.1007/978-3-319-00666-6_2
- Miall, A. D. 1977. "A Review of the Braided-River Depositional Environment." *Earth-Science Reviews* 13 (1): 1-62. [https://doi.org/10.1016/0012-8252\(77\)90055-1](https://doi.org/10.1016/0012-8252(77)90055-1)
- NQA 1 2012, "Quality Assurance Requirements for Nuclear Facility Application." American Society of Mechanical Engineers, New York, New York.
- Pirot, G., J. Straubhaar, and P. Renard. 2014. Simulation Of Braided River Elevation Model Time Series With Multiple-Point Statistics. *Geomorphology*, 214: 148-156. <http://dx.doi.org/10.1016/j.geomorph.2014.01.022>
- Pyrzc, M. J., J. B. Boisvert, and C. V. Deutsch. 2008. "A Library of Training Images for Fluvial and Deepwater Reservoirs and Associated Code." *Computers & Geosciences* 34 (5): 542-560. <https://doi.org/10.1016/j.cageo.2007.05.015>
- Robinson, J., T. Johnson, and M. Rockhold. 2019. "Feasibility Assessment of Long-Term Electrical Resistivity Monitoring of a Nitrate Plume." *Groundwater* 58 (2): 224-237. <https://doi.org/10.1111/gwat.12899>
- Robinson, J., J. Thomle, D. McFarland, K. Deters, M. Rockhold, F. Day-Lewis, and V. Freedman. 2022. "Integration of Large-Scale Electrical Imaging into Geological Framework Development and Refinement." *Environmental Processes* 9 (2). <https://doi.org/10.1007/s40710-022-00570-2>
- Rockhold, M. L., F. A. Spane, T. W. Wietsma, D. R. Newcomer, R. E. Clayton, I. Demirkanli, D. L. Saunders, M. J. Truex, M. M. Valenta-Snyder, and C. J. Thompson. 2018. Physical and Hydraulic Properties of Sediments from the 200-DV-1 Operable Unit. PNNL-27846, RPT-DVZ-CHPRC 0005, Rev. 0, Pacific Northwest National Laboratory, Richland, Washington.
- Rockhold, M. L., S. R. Waichler, J. L. Downs, X. He, J. D. Tagestad, Y. Fang, V. L. Freedman, M. J. Truex, and C. M. R. Yonkofski. 2019. Information on Technical Impracticability for Remediation of Iodine-129 Contamination – Summary of Data and Modeling for Hanford Site 200-UP-1 Operable Unit. PNNL-28057, Rev. 1.0, Pacific Northwest National Laboratory, Richland, Washington.

Serne, R. J., B. N. Bjornstad, J. M. Keller, P. D. Thorne, D. C. Lanigan, J. N. Christensen, and G. S. Thomas. 2010. Conceptual Models for Migration of Key Groundwater Contaminants through the Vadose Zone and Into the Unconfined Aquifer Below the B-Complex. PNNL-19277, Pacific Northwest National Laboratory, Richland, Washington.

Spane, F. A., and V. R. Vermeul. 1994. Summary and Evaluation of Hydraulic Property Data Available for the Hanford Site Upper Basalt Confined Aquifer System. PNL-10158, Pacific Northwest Laboratory, Richland, Washington.

Strait, S. R. and R. B. Mercer 1987. Hydraulic Property Data from Selected Test Zones on the Hanford Site. SD-BWI-DP-051, Rev.2, Rockwell Hanford Operations, Richland, WA.

Strebelle, S. 2002. "Conditional Simulation of Complex Geological Structures Using Multiple-Point Statistics." *Mathematical Geology* 34 (1): 1-21. <https://doi.org/10.1023/a:1014009426274>

Pacific Northwest National Laboratory

902 Battelle Boulevard
P.O. Box 999
Richland, WA 99354
1-888-375-PNNL (7665)

www.pnnl.gov